HHS Public Access

Author manuscript

Cancer Res. Author manuscript; available in PMC 2021 January 01.

Published in final edited form as:

Cancer Res. 2020 July 01; 80(13): 2940–2955. doi:10.1158/0008-5472.CAN-19-2331.

Cancer Exacerbates Chemotherapy-Induced Sensory Neuropathy

Stephen N. Housley[1], **Paul Nardelli**[1], **Dario I. Carrasco**[1], **Travis M. Rotterman**[1], **Emily Pfahl**[1], **Lilya V. Matyunina**[1,3], **John F. McDonald**[1,3], **Timothy C. Cope**[1,2,3]

[1]School of Biological Sciences, Georgia Institute of Technology, Atlanta, Georgia 30332.

[2]W.H. Coulter Department of Biomedical Engineering, Emory University and Georgia Institute of Technology, Georgia Institute of Technology, Atlanta, Georgia 30332.

[3]Integrated Cancer Research Center, Parker H. Petit Institute for Bioengineering and Bioscience, Georgia Institute of Technology, 315 Ferst Drive, Atlanta, GA, 30309, USA.

Abstract

For the constellation of neurological disorders known as chemotherapy-induced peripheral neuropathy, mechanistic understanding and treatment remain deficient. Here we present the first evidence that chronic sensory neuropathy depends on non-linear interactions between cancer and chemotherapy. Global transcriptional profiling of dorsal root ganglia revealed differential expression, notably in regulators of neuronal excitability, metabolism, and inflammatory responses, all of which were unpredictable from effects observed with either chemotherapy or cancer alone. Systemic interactions between cancer and chemotherapy also determined the extent of deficits in sensory encoding and ion channel protein expression by single mechanosensory neurons, with the potassium ion channel Kv3.3 emerging as one potential contributor to sensory neuron dysfunction. Validated measures of sensorimotor behavior in awake behaving animals revealed dysfunction after chronic chemotherapy treatment was exacerbated by cancer. Notably, errors in precise forelimb placement emerged as a novel behavioral deficit unpredicted by our previous study of chemotherapy alone. These original findings identify novel contributors to peripheral neuropathy and emphasize the fundamental dependence of neuropathy on the systemic interaction between chemotherapy and cancer.

Introduction

Chemotherapy can achieve high rates of survival in patients with common cancers (1) but often causes severe side effects, including neuropathy, that can limit its use (2, 3). Debilitating sensory disorders, including pain, paraesthesia, and somatosensory loss, reduce quality of life for many patients and can persist for months or years after discontinuing chemotherapy (4, 5). These neurological disorders occur for up to 80% of patients receiving commonly used antineoplastic agents, notably antitubulins and proteasome inhibitors, as well as platinum-based compounds (5, 6), which are the prescribed adjuvant treatment in

Corresponding Author: Timothy C. Cope, 555 14th St. NW. Atlanta, GA, 30318, Phone: (404) 385 4293, tim.cope@gatech.edu.

Conflict of Interests: The authors declare no conflicting interests.

50% of cancer cases worldwide (7, 8). There are few options available for the prevention or treatment of sensory disorders and those that exist largely focus on symptomatic management not prevention (9). Thus, there is an urgent need to better understand the pathogenesis of sensory dysfunction to aid development of mechanism-based therapies.

Preclinical studies of chronic neuropathy in experimental models of cancer are unavailable, possibly because of presumption that chemotherapy alone is sufficient to explain the neuropathology. A recently published meta-analysis identified 341 preclinical studies of chemotherapy induced neuropathy, and none assessed interaction between chemotherapy and cancer (10). Omitting cancer from preclinical study produces a fundamental gap in knowledge that may explain why treatments for neuropathic side effects of chemotherapy have been unsuccessful in patients with cancer. Cancerous tumors located outside the nervous system can induce cognitive disability and peripheral nervous system dysfunction independent of chemotherapy, surgery, or co-morbidities (11, 12). Moreover, cancer provokes dysregulation in immune, metabolic, oxidative and neuronal excitability (13, 14), all of which are identified as targets through which chemotherapy produces neuropathy (2). Convergence of cancer and chemotherapy on the same biological processes seems likely to yield non-linear interactions, leading us to hypothesize that clinically relevant neuropathy emerges from codependent actions of cancer and chemotherapy.

We tested our hypothesis by uncoupling the independent and combinatorial effects of cancer and chemotherapy on sensory neurons in studies of rats that are not feasible in human patients. Here we present original findings to show that sensory neuropathy depends on complex systemic interactions between cancer and chemotherapy. By combining cancer and chemotherapy, we reproduce the relevant clinical condition in preclinical study of rats to produce the first transcriptional profile of nervous tissue, to discover recurrent metabolic reprogramming and perturbed inflammatory and ion channel processes distinct from the independent effects of cancer or chemotherapy. Parallel codependency is found in novel neuropathic responses of mechanosensory neurons, both in their immunohistochemistry for selected voltage-gated potassium ion channels and in electrophysiological measures of encoding naturalistic stimuli *in vivo*. Collectively, our data show for the first time that sensory neuropathy emerges from codependencies between the systemic effects of cancer and chemotherapy. Apart from identifying new molecular targets for restoring function to mechanosensory neurons, our findings provide the fundamental insight that accounting for chemotherapy-cancer combinatorial effects on the somatosensory nervous system is prerequisite for developing meaningful treatment or prevention of neuropathy.

Methods

Animal Care

All procedures and experiments were approved by the Georgia Institute of Technology Institutional Animal Care and Use Committee. Adult male rats (250–350g) were studied in terminal experiments only and were not subject to any other experimental procedures. All animals were housed in clean cages and provided food and water ad libitum in a temperature- and light-controlled environment in Georgia Institute of Technology's Animal facility.

Rat model of Colorectal Cancer

We studied the rat model of colorectal cancer developed in Fisher 344 (F344) rats and known as polyposis in rat colon ($Apc^{Pirc/+}$) (15). Pirc rats generated from a germline mutation in the Apc gene ($Apcam^{1137/+}$) approximate human colorectal cancer. We studied age-matched male rats (4 months). This age has been previously validated to result in 100% incidence of animals (16) developing colon cancer and was consistent with our population (Fig. S1). $Apc^{Pirc/+}$ rats exhibit: regional distribution of tumors that best represents that seen in human colorectal cancer (16); histopathology and morphology closely resembling human tumors (adenocarcinomas) (17), up-regulation of well-established pro-growth factors, e.g. β-catenin and EGFR and proliferative makers Ki-67 seen in human carcinogenesis (Fig. S1) (15), dramatic increases in Wnt signaling believed to be a key factor in human colorectal carcinogenesis, presence of apoptotic resistant cells unique to carcinogenesis (15, 16), oxaliplatin (OX)-induction of apoptosis in colon tumors, survivability (12–15 months) enabling long-term investigation of OX's chronic effects (15).

Chemotherapy treatment

OX was injected i.p. once a week (10mg/Kg, 1 ml 5% dextrose in DMSO) in aged matched rats (4 months) to achieve a cumulative dose of 70 mg/Kg over 7 weeks (Fig. 1a), which scales to a human dose of 420mg/m2 (conversion based on rat body surface area and Km= 6) (18). This dose minimizes nerve degeneration in patients (19, 20). Throughout the entirety of the experimental timeline, rats were visually and physically (palpation) inspected for pain, distress, or signs of local infection. No individual rat reached set criteria established for early removal from the study: greater than 10% weight loss, pain or distress assessed by vocalization, absence of grooming, and rats show normal exploratory and feeding behaviors (Fig. S2). In contrast with previous reports, (21) no animals exhibited signs of local inflammation, bloating or infection, nor did we find any evidence of fibrino-purulent peritonitis during necropsy to recover tumors and other tissues.

Surgical Procedures

Terminal in vivo experiments were performed 5 weeks after achieving clinically relevant chemotherapy doses. They were designed to measure the firing of individual intact sensory neurons in response to physiologically relevant muscle contraction and stretch with electrophysiological techniques. All in vivo procedures are well established in our lab and have been extensively described in previous publications (22–24). Briefly, rats were deeply anesthetized by inhalation of isoflurane (5% in 100% O_2), intubated via a tracheal cannula, then maintained for the remainder of the experiment (up to 12 hours by 1.5–2.5% in 100% O2). Respiratory rate, pCO_2, core temperature, pulse rate and pO_2 were continuously monitored and maintained by adjusting anesthesia and adjusting heat sources. Dorsal roots (lumbar L4–6), muscles, and nerves in the left hindlimb were prepared for stimulation and recording with the rat fixed in a rigid frame at the snout, vertebral bodies, distal tibia, and distal femur (knee angle 120°). Triceps surae muscles (lateral and medial gastrocnemii and soleus) were partially freed of surrounding connective tissue and marked for their resting length (L_o) at ankle angle 90° before their common Achilles tendon was severed at the calcaneus and tied directly to the lever arm of a force- and length-sensing servomotor

(model 305B-LR; Aurora Scientific). Triceps surae nerves were loosely positioned in continuity on a unipolar silver stimulating electrode, and all other hindlimb nerves were crushed to reduce extraneous neuronal activity. Dorsal rootlets were carefully freed in continuity from overlying connective tissue and supported on bipolar hook electrodes positioned close to the rootlet's entry into the dorsal spinal cord. Exposed tissues were covered with warm mineral oil in pools formed by attaching the edges of severed skin to the recording frame.

In vivo Intracellular Recording

Dorsal rootlets positioned in continuity on bipolar recording electrodes were selected for sampling sensory neurons when they produced robust action potential activity in response to stretch of triceps surae muscles. Individual axons penetrated in these rootlets by glass micropipettes (~30 MΩ filled with 2 M K+ acetate) were selected for study when electrical stimulation of triceps surae nerves produced orthodromic action potentials that were readily resolvable and had conduction delay of <2ms. Continuous intracellular recordings from sensory neurons were acquired with Spike2 software (version 8.02). Sensory neurons were classified as Ia by their perfect entrainment to 1-s bouts of high-frequency, small-amplitude vibration (100Hz, 80 μm), pause in firing during rising twitch force response (muscle shortening), and by responding with an initial burst of high-frequency firing (>100 pulses per second (pps)) at the onset of muscle stretch (24). Two stretch paradigms were used to characterize the firing responses of afferents to physiologically relevant mechanical stimuli. In both paradigms, triceps surae muscles were stretched by 3 mm from L_o (7% strain). Ramp-hold-release stretches tested afferent encoding of both fast dynamic (20mm/s, 47% strain rate) and static stimuli; successive triplets of triangular stretch tested slow (4mm/s, 9% strain rate) dynamic and activity-dependent encoding in dynamic stretch known to be influenced by recent signaling history (24). Strains and strain-rates fall within values expected for animals engaged in normal activities e.g. locomotion, and have been previously used in our lab (24).

Tissue Collection

At the conclusion of data collection, rats were overdosed with isoflurane inhalation (5%) then immediately transcardially perfused with cold vascular rinse (0.01 M PBS pH 7.4) followed by room temperature fixative (2% paraformaldehyde in 0.1 M PBS, pH 7.4). Muscles and dorsal root ganglia were quickly dissected and post-fixed for one hour in the same fixative. After a brief wash in a 0.1 M PBS, tissues were incubated in 0.1 M PBS containing 20% sucrose at 4°C overnight. Three to four animals from each of four groups were selected for whole-transcriptome analysis alone and did not undergo further analysis. Dorsal root ganglia (DRG) from the lumbosacral (L5-S2) spinal cord were surgically removed (4–6 per animal), washed with sterile saline and immediately flash frozen (fresh) in 2-methylbutane (isopentane) pre-chilled in liquid nitrogen. DRG were then stored at −80°C for further analysis (see below). After DRG removal, colonic tumors from $Apc^{Pirc/+}$ rats were dissected and counted prior to post fixation for immunohistochemical analysis.

Immunohistochemistry and Imaging

Details of our immunohistochemistry procedures have been previously described (25). Briefly, 50-μm thick sections of skeletal muscles, DRGs, and tumors were cut using a Cryostat (Leica). Tissues sections from all treatment groups were processed simultaneously. All tissue sections were incubated overnight in primary antibodies diluted in blocking buffer (5% normal goat serum, 0.3% Triton100 in PBS). The primary antibodies used were as follow: rabbit polyclonal anti-NaV1.6 (ASC-009, Alomone Laboratories, 1:200), rabbit polyclonal anti-NaV1.1 (ASC-001, Alomone Laboratories, 1:300), rabbit polyclonal anti-NaV1.7 (ASC-008, Alomone Laboratories,1:100), rabbit polyclonal anti-Kv3.3 (APC-102, Alomone Laboratories, 1:300), mouse monoclonal anti-Kv1.1 (K36/, NeuroMab, University of California Davis, 1:300), guinea pig polyclonal anti-VGLUT1 (135–104 Synaptic Systems, 1:300), chicken polyclonal anti-neurofilament protein (NF-H, Aves Laboratories, 1:200), mouse monoclonal anti-ASIC2, (E-20, Santa Cruz Biotechnologies,1:200), mouse monoclonal anti-EGRF (SC-120, Santa Cruz Biotechnolgy, 1:100), mouse monoclonal anti-KI67 (SC-23900, Santa Cruz Biotechnology, 1:100), mouse monoclonal anti-IL6 (SC-57315, Santa Cruz Biotechnology, 1:100). After washing with PBS, tissue sections were incubated with appropriate fluorescent-conjugated secondary antibodies (Jackson ImmunoResearch Laboratories), diluted in blocking buffer, for 1 hr. at room temperature. Following washes with PBS, slides were mounted using Vectashield containing DAPI (Vector Laboratories) in order to label cell nuclei.

RNA Extraction and Amplification

RNA extraction and amplification were performed according to our previously described methods (26). Briefly, RNAs were isolated and purified from sensory neurons of DRG (L5-S2) using the mRNeasy Micro KIT (Qiagen, Germantown, MD). Total RNA concentration and integrity was assessed on the Bioanalyzer RNA Pico Chip (Agilent Technologies, Santa Clara, CA). Labeling of RNAs was performed with the FlashTag Biotin HSR RNA Labeling Kit (Affymetrix, ThermoFisher). Gene expression was determined by microarray analysis on the Affymetrix platform (Rat Transcriptome Array 2.0).

Microarray data analysis

In total, 13 (four groups with biologic triplicates per group (4 biologic replicates from $Apc^{Pirc/+}$+OX group) global transcriptional expression data sets were generated in this study. Raw mRNA expression data were processed using Affymetrix Expression Console (EC) software Version 1.4. Raw data probes were normalized using SST-RMA algorithm. Differentially expressed genes (DEG) were determined through a linear fixed effects model (*limma* (27)) with a robust empirical Bayes (eBayes) framework to moderate the residual variances (27). This has the effect of increasing the effective degrees of freedom by which gene-wise variances are estimated, thus reduces the number of false positives for genes with small variances and improves power to detect DEG with larger variances (28).

Unsupervised multivariate analysis

DEGs were subjected to paired multivariate analysis to discover high-level data structure. By serially linking two analytic techniques, Principal Components Analysis (PCA) driven

Hierarchical clustering, we stabilize clustering performance and reduced dimensionality to tractably few continuous variables containing the most important information on which clustering algorithms are focused which leads to a better clustering solution (29, 30). PCA and visualization was applied to DEGs with the *factoextra* (31) and *FactoMineR* (29) packages. PCs capturing high-level structure were then employed to drive hierarchical clustering. Hierarchical clustering and heatmaps were visualization with the *gplots* package (*heatmap.2*) (32) in the R environment (3.5.0). Hierarchical-clustering, using the ward.D2 method (33) were applied to the eBayes-filtered gene set to obtain unsupervised visualization of the gene clusters coordinately expressed among the different experimental groups. Prior to hierarchical clustering, genes were standardized across the samples to a mean of zero and an s.d. of 1. Subclusters were derived using the R function *cutree* (34).

Pathway and Gene Set Enrichment Analysis

Hypergeometric testing was conducted on subclusters of named genes using DAVID (Database for Annotation, Visualization, and Integrated Discovery) and g:Profiler to pinpoint significantly enriched pathways or gene ontology terms (35). We increase statistical power by hypergeometric testing on subclusters which separates co-regulated (up or down) probe sets (36). All biological processes with adjusted $P < 0.05$ were considered significantly enriched. g:Profiler 3–500 (min-max) Benjamini Hochberg FDR correction intersection terms (2) only annotated genes were searched.

Parallel identification of pathways enrichment was performed by GSEA (gene-set enrichment analysis). GSEA uncovers novel sets of functionally related genes by focusing on all detected (above-background) genes. GSEA is unbiased and more sensitive, thus allowing for the detection of even subtle enrichment signals. The Molecular Signature Database v 6.2 (C2-CP: canonical pathways; C3- MIR: microRNA targets; C3- TFT: transcription factor targets; C5-BP: GO biological process; C5- CC: GO cellular component; C5- MF: GO molecular function C7: immunologic signatures gene sets) with the permutation type set to ‘gene set,’ 15–500 (min-max), to calculate statistical significance, as suggested for fewer than seven replicates; default settings were applied to all the other options. For GSEA, a false discovery rate (FDR) of <0.2 was considered statistically significant.

Targeted Transcriptional Analysis

Complementary supervised analysis of DEGs leveraged knowledge of proteins known to be expressed at sensory neuron receptor endings that directly (25, 37, 38) or indirectly (39, 40) regulate excitability. In addition, due to incomplete knowledge of the full suite of proteins that are necessary and sufficient for normal function (40), we expand targeted transcriptional analysis to incorporate gene families, including: ion channels, GPCRs, and channel regulators.

3D Digital Reconstructions and Anatomical Quantifications

Z-axis stacks of images of muscle spindles receptor endings, DRGs and tumors were constructed by sequentially imaging using a confocal microscope (LSM 700A, Zeiss). Muscle spindles terminals z-stacks (1μm steps) were captured with a 40X oil immersion

objective (N.A 0.6) at 0.6 digital zoom. DRG and tumors z-stacks (1μm steps) were captured with a 20X objective (N.A 0.4) at 0.6 digital zoom. Stacks of images were processed and analyzed using Amaris (Bitplane) or imageJ (NIH) imaging software. Figures present images as flat maximal projections of the sum of the z-axis optical slices. Analysis of neuron receptor endings (spindles) and soma (DRG) were performed by an investigator blinded to treatment group. Immunoreactivity in nerve terminals and DRG was determined by measuring the mean pixel intensity of on each en-face portions of the terminal (visualized by the VGLUT1 staining) observed on every 1 um single image or on the medium and large size cell somas observed on the flat maximal projections of the z-stacks images respectively.

Intracellular Recording Pre-Processing

Intra-axonal recordings of action potentials together with records of muscle length and force were digitized (20 kHz) and were monitored online and stored on computer for later analysis with Spike2 and custom-written MATLAB scripts. From raw intracellular data of both paradigms, we extracted 31 measured and derived features (Fig. S3) that provide a comprehensive quantification of neuronal signaling characteristics. We then categorized features into four broad clusters that represent functional features encoded by these neurons, containing sensitivity (Thr), dynamic (Dyn), static (Stat), and history-dependent (Hx) signaling information. Fig. S3 identifies and describes the measured and computed features and functional clustering used for inference.

Statistical Analysis of Intracellular Recordings

Linear discriminant analysis (LDA) provided supervised dimensionality reduction for the multiple features of neuron signaling, in an attempt to find a linear combination of features that separated and characterized independent and combinatorial treatment effects. Data were first de-meaned, normalized to unit standard deviation, and tested by Bayesian one-way ANOVA (*stan_glm*) (41). The derived covariance matrix was then normalized by within-group, pooled covariance. The eigenvectors of that modified covariance matrix defined three canonical variables that characterized and separated the four treatment groups identified *a priori* as Apc^{WT}+control, Apc^{WT}+OX, $Apc^{Pirc/+}$+control, *and* $Apc^{Pirc/+}$+OX. LDA and 10-fold cross validation of model performance (repeated holdout method) was performed with the *MASS* (7.3–51.1) library in the R environment (3.5.0). Individual features characterizing the firing responses of neurons sampled from multiple rats were tested for statistically significant differences with Bayesian one-way ANOVA (*stan_glm*). Bayesian parameters estimation derives the entire joint posterior distribution of all parameters simultaneously thus circumventing the need to correct for multiple tests on the data.

Bayesian hypothesis testing was performed by analyzing the probability mass of the parameter region in question. This leads to a direct probability measure that defines values inside the 95% of the highest posterior density (HDI) more credible than outside values. HDI was used to make unbiased inferences by directly comparing the posterior probability distributions between two (or more) contrasts of interests e.g. mean-comparisons testing. For example, an HDI of a credible difference distribution that does not span zero indicates that the model predictions for the two conditions of interest are different from each other resulting in evidential support that parameters for both populations are unequal.

Bayesian Models

All models were developed in fully hierarchal Bayesian framework (Fig. S4) with the *rstanarm* package (2.18.1) (41) in the R environment (3.5.0). *Rstanarm* implements regression models in *stan*, which are fit using Hamiltonian Markov Chain Monte Carlo sampling to compute credible parameter values (42, 43). For intercepts and predictors, we use Student's *t*-distribution with mean zero and four degrees of freedom as the prior distribution. The scale of the prior distribution is 10 for the intercept and 2.5 for the predictors. Each model was run with four independent chains for 400 warm-up, 4,000 sampling steps and every second sample (thinning) was discarded. For all parameters, the number of effective (*n_eff*) samples was >500. Convergence was assessed and assumed to have reached the stationary distribution by ensuring that the Gelman–Rubin shrinkage statistic (rhat, $\hat{R}$) statistic for all reported parameters was <1.05 (and Monte Carlo standard error of the parameter means was <0.002 (44). We report the expected mean parameter values alongside 95% credible intervals using the HDI (Fig. S5)

Bayesian Model Validation

Models performance was validated (Fig. S5) by computing out-of-sample predictive accuracy using Pareto-smoothed importance sampling (PSIS) to perform leave-one-out cross (LOO) validation. Although alternative validation strategies (WAIC) are asymptotically equal to LOO, PSIS-LOO provides a more accurate and stable estimate of model performance and is more robust in the finite cases with diffuse priors (weakly informative). We obtained standard errors for predictions and for comparison of predictive errors between models to definitively test and rank models based on predictive accuracy (*elpd* = expected log pointwise predictive density).

Behavioral analysis

We used the ladder rung walking task as a validated outcome to detect and describe sensorimotor deficits (45). The ladder rung apparatus was built as previously described (45). Secure hind foot placement was assessed using the seven-category scale scoring system introduced by Metz and Whishaw (45) with modifications as to not distinguish whether or not an error was associated with a deep fall. The total number of errors in forelimb and hindlimb placement was calculated and the mean error/step ratio was calculated per animal and represented as percent of error where an increase in the number of errors/steps corresponds to a decrease in secure foot placement of the hind and/or fore foot.

Data and material availability

Microarray datasets supporting the conclusions of this article are available in the Gene Expression Omnibus (GEO) repository under accession code: GSE126773. Data supporting the conclusions of this article are included within the article and its Supplementary Files. Other datasets, code, and models that support the findings of this study are available from the corresponding author upon reasonable request.

Results

Transcriptional profiling of sensory neurons

We first profiled the transcriptomes of lumbosacral (L4-S1) dorsal root ganglia (DRG), where sensory neurons (Fig. 1b) are vulnerable to chemotherapy (2). We studied wild-type (Apc^{WT}) rats and rats carrying an *Apc gene* mutation ($Apc^{Pirc/+}$) (15) associated with development of colon cancer (Fig. S1 (46)), not only in these rats, but also in 80% of patients with colorectal cancer (46)). Presence of malignant colonic tumor burden was validated in all $Apc^{Pirc/+}$ rats by immunohistochemical evaluation of key indicators of malignancy, e.g. Ki67 and EGFR (Fig. S1) from tumors collected during terminal experiment dissection. Rats in each group were randomized to receive injections of oxaliplatin (OX), a platinum based compound known to induce neuropathy in patients with cancer and shown in our previous studies to induce chronic movement disorders (23). OX was administered by intraperitoneal injection on a human-scaled dose schedule (Fig. 1a) (23). The OX treatment schedule resulted in four experimental groups used for all studies: Apc^{WT}+control, Apc^{WT}+OX, $Apc^{Pirc/+}$+control and $Apc^{Pirc/+}$+ OX (Fig. 1a).

We employed an empirical Bayesian (eBayes) linear model (27) to modify residual variances on a total of 31,042 (22,875 named) genes and identified 3,426 differentially expressed genes (DEG) across all groupwise contrasts ($P_{\text{eBayesAdj}} < 0.005$). Subsequent *post hoc* analysis identified DEG from all possible contrasts (fold-change (FC) ≥1.2 and ≤−1.2). Overlap between DEGs retrieved from individual comparisons is illustrated in Figure 1c. In keeping with the notion that chemotherapy and cancer act through similar molecular mechanisms, we found overlap of 112 DEG affected independently by cancer and chemotherapy (Fig. 1c). Of note, we found that 73.8% (n=1,704) of all DEG (n=2,307) were uniquely affected when cancer and chemotherapy interacted ($Apc^{Pirc/+}$+OX) (Fig. 1c). Figure 1d lists the top DEG (FC ≥ 4 and ≤ −4) identified in $Apc^{Pirc/+}$+OX in comparison to the effects observed in Apc^{WT}+OX or $Apc^{Pirc/+}$+control. Collectively, these findings demonstrate the first evidence that cancer exacerbates genetic dysregulation induced by chemotherapy, unmasking a more than four-fold increase in DEG.

Next, we performed two independent downstream analyses (Fig. S6) to test for interaction and determine which biologic processes might be involved in pathogenesis of sensory disorders. First, we subjected the eBayes filtered database to unsupervised principal component (PC) analysis. DEG were visualized in the new 3D composite space created by PC1–3 (Fig. 1e) that explained 83.98% of the variance and clearly segregated the four experimental groups. Inspection of individual PCs revealed significant evidence of non-linear interactions between cancer and chemotherapy captured in PC1 (65.6% of explained variance), whereas PC2 (11.14%) and PC3 (7.24%) separated the effects of cancer and chemotherapy, respectively (Fig. 1f). Second, we drove unsupervised hierarchical clustering onto the PC1 solution to identify groups of coregulated genes that express interaction (Fig. 2a). Analysis identified two clusters of genes displaying distinct, but internally consistent expression profiles clearly representing patterns of interaction (Fig. 2a, C1 and C2; Table S1).

We then subjected clusters of named genes (Table S1) to pathway-enrichment analysis (35) and identified unique subclusters (Fig. 2a) expressing dysregulation in distinct biological processes (Fig. 2b). In keeping with the notion that combinatorial effects of cancer and chemotherapy (OX) reflect convergence onto shared signaling pathways, genes mediating inflammatory response, e.g. interleukin 6 (*Il6)* ($P_{\text{eBayesAdj}}$=7.82× 10^{-6}), *Ptgs2* ($P_{\text{eBayesAdj}}$=0.0028) and *Cxcr4* ($P_{\text{eBayesAdj}}$=3.74× 10^{-7}), and reactive oxygen species processes, e.g. *Hmbox1* ($P_{\text{eBayesAdj}}$=0.001), were found to be among the most upregulated in cluster 1a (C1a) (Fig. 2b). Notably, we observed substantial induction of genes encoding glycolytic and carbohydrate metabolic processes (FDR ≤ 1.83×10^{-3}, C1a; Fig. 2b) in the $Apc^{Pirc/+}$+OX neurons. Coincident with these changes was a statistically significant down-regulation of genes mediating lipid metabolism (C2a), suggestive of pervasive metabolic dysfunction beyond the small subset of dysregulated mitochondrial related processes that we found in response to Apc^{WT}+OX or $Apc^{Pirc/+}$+control alone (Fig. 2b; Fig. S7a,b) and similar to dysfunctional effects previously suggested (2). Among additional unique transcripts downregulated in $Apc^{Pirc/+}$+OX neurons, Fig. 2b highlights multiple deficits in processes related to extracellular matrix control, mechanical stimulus transduction, (C2a), DNA-binding, RNA polymerization, (C2b), transcription factor activity, hormone signal transduction (C2c and Table. S1). Furthermore, we observed genes in C1b and 2a that represent specific dysregulation of neuronal and sensorimotor function, e.g. ion-channel genes determining neuronal excitability along with coincident down-regulation of locomotion. These data provide the first evidence that codependent neuropathy induces broad metabolic reprogramming, e.g. increased glycolytic and decreased lipid metabolism, consistent with cancers capacity to corrupt metabolic processes (47, 48), which extends knowledge beyond the limited impairment observed in mitochondria (Fig. S8).

Markers for nerve degeneration, inconsistently observed in patients treated with antineoplastic drugs (49) exhibited mixed results. While we observed few significantly downregulated genes associated with myelination processes (C2b; $P \leq 7.12\times10^{-3}$, Fig. 2b), we also found significant induction of processes involved in the preservation of neurons (e.g. enrichment of negative regulation of apoptosis $P \leq 5.96 \times 10^{-3}$) in C1a. Mixed results from these data suggests heterogeneous neuronal populations in the DRG may contain discrete subpopulations with selective vulnerability whereas others are resistant to degeneration, which is consistent with mixed results seen in human studies (49) and highlights the need for future cell-type specific investigations that are currently unavailable.

Dysregulation is conserved at protein level

Because inflammatory pathways play multiple roles in regulating neuron function (50), we focused attention on their significant response to codependent neuropathy. We selected the most dysregulated gene in the inflammatory pathways, *Il6*, for molecular validation by assessing gene—protein correspondence. Sensory neurons in dorsal root ganglia were immunolabeled with monoclonal antibodies targeting IL6 (Fig. 2c). As predicted from the transcriptional profiling (Fig. 2d), the IL6 protein was constitutively expressed in Apc^{WT} +control rats at lower levels than in $Apc^{Pirc/+}$ control animals or Apc^{WT}+OX animals, and at significantly higher levels in $Apc^{Pirc/+}$+OX neurons (Fig. 2e), demonstrating that codependent neuropathy was conserved in protein expression (Fig. 2e and Fig. S9). Previous

studies implicate IL6's capacity to mediate hyperexcitability and morphological changes associated with neuron death (51). However, studies restricted investigation to acute neurotoxicity, which limits generalizability to symptoms that persist long after treatment. Our data present the first evidence that *Il6* (IL6) expression levels remain elevated long after treatment cessation without observable morphological changes. We show that codependent neuropathy significantly increases *Il6* (IL6) when compared to chemotherapy or cancer alone. In light of IL6's capacity to decrease excitability following chronic exposure (51), our data suggest that neuronal dysfunction (see below) as a result of codependent neuropathy may be expressed as hypo-excitability, in contrast with previous work (5).

Global dysregulation of neuron transcriptomes

We then used gene-set enrichment analysis (GSEA) as a second independent tool to investigate the cellular processes underlying codependent neuropathy. We initially focused on the comparison of Apc^{WT}+OX and $Apc^{Pirc/+}$+OX (Fig. 3a) and $Apc^{Pirc/+}$+control and $Apc^{Pirc/+}$+OX (Fig. 3b) and interrogated entire data sets against the Molecular Signatures Database (Table S2). Two novel conclusions can be drawn from the GSEA findings. First, GSEA independently validated codependencies of cancer and chemotherapy in the DEG identified by transcriptional profiling using paired unsupervised analysis (Figs. 3a and 3b). GSEA corroborated downregulation of lipid metabolic pathways (normalized enrichment score (NES)=1.73) and upregulation of glycolytic pathways (NES=−1.94) in $Apc^{Pirc/+}$+OX sensory neurons when compared with either chemotherapy (Fig. 3a) or cancer alone (Fig. 3b). Focusing analysis on pathways directly involved in neuronal signaling confirmed dysfunction in peripheral neuron ensheathment in the absence of evidence supporting neuron specific apoptotic response (FDR>0.83) (Fig. 3a). Second, GSEA exposed dysregulation of genes relevant to neuronal excitability particularly potassium ion channels and transporters, and others participating in synaptic communication, e.g. SNARE and glutamatergic transmission (Fig. 3a, b). Dysregulation of these and other gene sets (e.g. proinflammatory chemokines) was not predicted from the independent effects of cancer or chemotherapy alone. (Table S2). Unlike previous studies that consistently report dysregulated voltage-gated sodium channels (52), we find little evidence of differentially expressed sodium channels or disrupted regulatory pathways (52). Instead, we find targeted DEG related to potassium ion channels unlike those previously identified. We draw two conclusions from these data. First, ion channel clusters are differentially vulnerable to codependent neuropathy. Second, chronic neuropathy may be mechanistically linked to dysregulation of ion channels distinct from those identified in acute preparations.

Taken together, our analyses indicate significant dysregulation of genes and proteins mediating core cellular processes of $Apc^{Pirc/+}$+OX sensory neurons. Our integrated transcriptomics and protein level findings confirmed that cancer and chemotherapy effect common processes (13, 53, 54). Moreover, our findings support our central hypothesis that clinically relevant neuropathy depends on systemic interaction between cancer and chemotherapy by showing for the first time that codependence exacerbates neuropathy and revealing it operates through distinct mechanistic pathways, unpredicted from cancer or chemotherapy alone.

Novel voltage-gated ion channel dysfunction

Sensory deficits, e.g. somatosensory and hearing loss, are commonly reported by patients long after cessation of chemotherapy, but knowledge of the combined effects of cancer and chemotherapy is missing. Mechanosensory systems, e.g. cochlear hair cells, and various somatosensory neurons in skin and muscle are responsible for encoding this information and exhibit deficits following chemotherapy (6). We therefore next focused on identifying the combined effects of cancer and chemotherapy on a representative member of mechanosensory neurons, called muscle spindles. Muscle spindles share many of the molecular mechanisms (40) underlying mechanotransduction and encoding found in this broad class of sensory neurons (e.g. hair cells (55), Merkel (56)). Further, signaling by these neurons encodes sensory features of muscle mechanics necessary for perceiving (proprioception) and coordinating body position and movement, functions which, when impaired, have the potential to explain persistent disorders in patients (57). We performed targeted analyses of our transcriptome database by querying DEGs identified in $Apc^{Pirc/+}$ +OX rats compared to all other groups against genes encoding proteins known to be constitutively expressed in mechanosensory neurons that mediate unique contributions to neuronal signaling (Fig. S10) (25, 37, 40). We found no evidence for independent nor combinatorial effects of cancer or chemotherapy at the genetic level (Fig. 4a) for channels mediating mechanotransduction (e.g. *Asic2*, *Piezo2*, *ENaCs*), signal amplification, and spike encoding (e.g. *Scn1a* (Nav1.1), *Scn8a* (Nav1.6), *Scn9a* (Nav1.7), *Cacna1s,-c,-d, -f (*Cav1.1–4), *Kcnn2* (SK2), *Kcna1* (Kv1.1))

Next, we performed cell-specific immunohistochemical analyses to test gene–protein correspondence. We found no evidence to suggest dysregulated protein expression nor did evidence emerge to suggest altered protein distributions (Fig. S11–13) for most proteins, including those mediating mechanotransduction (ASIC2), signal amplification (Nav1.1, Nav1.6, Nav1.7), spike encoding (Kv1.1), and mechanosensory sensitivity (VGLUT1). These findings demonstrate that many of the molecular mechanisms responsible for mechanotransduction and determining excitability of mechanosensory neurons were preserved in the $Apc^{Pirc/+}$+OX rats. These findings narrow the field of candidate mechanisms for which treatment might reasonably restore normal function.

Having exhausted examination of proteins known to be expressed in mechanosensory neurons, we extended our search to include ion channels yet to be identified, but known to regulate neuronal signaling in other classes of neurons (58–60). As one of the most dysregulated voltage-gated ion channels, *Kcnc3* (encoding protein Kv3.3) emerged as a novel candidate (Fig. 4a, b, Fig. S14). Pharmacologic and genetic perturbation of Kv3.3 (*Kcnc3*) impairs neuronal signaling (60) and is causally linked to ataxias (61) that are consistent with functional deficits observed in patients with cancer long after cessation of chemotherapy. We then immunolabeled sensory cell bodies in dorsal root ganglia and their receptor endings taken from Apc^{WT}+control with monoclonal antibodies targeting Kv3.3, which revealed the first evidence of this ion channel in all large diameter cell bodies in the dorsal root ganglia that supply mechanosensors (Fig. 4c Fig. S15) and endings (Fig. 4e). Results of comparison across experimental groups indicate that Kv3.3 expression was significantly lower in $Apc^{Pirc/+}$+OX compared with Apc^{WT}+control (Fig. 4d,), $Apc^{Pirc/+}$

+control, or Apc^{WT}+OX (Fig. S15), demonstrating that codependent dysfunction is conserved in cell-type specific protein expression. Moreover, conserved Kv3.3 expression in neuromuscular junctions suggests that Kv3.3 dysfunction was constrained to sensory neurons (Fig. S16). This is the first evidence implicating Kv3.3 in the development of neuropathy and the first data, to our knowledge, demonstrating a channelopathy persists long after treatment cessation. The capacity of Kv3.3 to drive fast spiking and to enhance transmitter release – processes that are required for mechanotransduction and spike encoding–suggests that this ion channel might provide both a potential novel mechanism for the dysfunction of mechanosensory neurons and a potential target for therapy.

Neuronal signaling is impaired

Next, we examined whether the codependent neuropathy we discovered at gene and protein levels had negative consequences on mechanosensory function in living animals. (Fig. S17). Applying electrophysiological methods to rats in vivo, we recorded spiking activity from single mechanosensory neurons responding to naturalistic mechanical stimuli (Fig. 5a). From these spiking responses, we collected 31 measured and derived parameters (average of four trials; n = 11 Apc^{WT}+control, n=19 Apc^{WT}+OX, n=20 $Apc^{Pirc/+}$+control, n = 10 $Apc^{Pirc/+}$+OX; Fig. S3) from which we extract four functional features encoded by these neurons, sensitivity, dynamic, static, and history-dependent signaling information (Fig. S3). In Apc^{WT}+control rats, we found that muscle stretch elicited the spiking expected from sensory neurons in normal animals (24) and humans (62), specifically high frequency initial bursting at stimulus onset, increasing dynamic firing during increasing stimulus, sustained static firing with slow accommodation during the hold phase of stretch (Fig. 5b), and history-dependent reduction in spike number (Fig. S18).

We next tested whether $Apc^{Pirc/+}$ or OX treatment alone induce signaling dysfunction. Although we find transcriptional dysregulation in $Apc^{Pirc/+}$+control (Fig. 1c and Fig. S7a), we found a remarkable degree of concordance with signaling in Apc^{WT}+control (Fig. 5b). $Apc^{Pirc/+}$+control neuronal signaling displayed comparable sensitivity to stimuli and showed similar static behavior across all neurons (n = 20; Fig. 5b,c) as the Apc^{WT}+control. We then found that OX treatment of Apc^{WT} rats induced mild signaling deficits that were less pronounced, occurred in a small proportion of neurons (5/19), and were primarily restricted to sensitivity functional clusters (Fig. 5b,c and Fig. S19d), validating our previous findings of restricted deficits observed in a different strain of healthy rats treated with OX alone (23).

In contrast to the observations in Apc^{WT}+control, Apc^{WT}+OX, or $Apc^{Pirc/+}$+control rats, we found drastically impaired neuronal signaling in $Apc^{Pirc/+}$+OX rats (Fig. 5b). High frequency initial bursting was attenuated four-fold and sensitivity to stimuli was reduced by three-fold at both high (Fig. S19d) and low velocity stretch (Fig. S18, S19d). During dynamic stimuli, we found marked reduction in the number of spikes over both stretch conditions (Fig. 5c). Neurons in $Apc^{Pirc/+}$+OX rats also failed to sustain firing (Fig. 5b). In addition, we observed fewer spikes (Fig. 5c) during rapid accommodation immediately preceding signal deletion, despite constant stimulus (Fig. 5b). We then simulated naturalistic compensation by subjecting $Apc^{Pirc/+}$+OX neurons to repeated trials at 1, 2, and 3x background stimulus (L_o strain) intensity, which failed to completely rescue signaling back

to Apc^{WT}+control levels (Fig. S20b,c,d). These data are the first to directly demonstrate a damaging functional interaction between the systemic effects of cancer and chemotherapy in sensory neurons in a living animal. While validating our previous findings of signaling deficits in chemotherapy alone (23), these data indicate that restrictive signaling deficits induced by chemotherapy or cancer alone were insufficient to reproduce the magnitude, direction and number of dysfunctional parameters induced by codependent neuropathy.

Dysfunction does not depend on degeneration

We next tested whether the impaired neuronal signaling of $Apc^{Pirc/+}$+OX neurons might be explained by dying-back degeneration of sensory nerve terminals. While the underlying mechanisms for chemotherapy induced neuropathy are not understood, current opinion identifies ‘dying-back’ axon degeneration as a major pathology in this disorder (19). Blinded reviewers assessed the structural integrity of sensory afferents and receptor endings immunolabeled against neurofilament protein (NEFH) (25). We then tested for functional evidence of degeneration by comparing differences in conduction delays, a physical measure of nerve degeneration that is used clinically (49). Neither histological observation of sensory afferents and receptors (Fig. 5d) nor axon conduction tests (Fig. S21) revealed evidence of dying-back degeneration of sensory nerve terminals ($Apc^{Pirc/+}$+OX: 1.41±0.13ms, n=10. Apc^{WT}+control: 1.52±0.14ms, n=11, Fig. S21). Our findings demonstrate that transcriptional changes we observed for some markers of nerve degeneration (Fig. 3) were insufficient to yield nerve degeneration. While our results indicate selective resistance of mechanosensory neurons in $Apc^{Pirc/+}$+OX rats, they are in line with the inconsistency of physical evidence for nerve degeneration reported in clinical studies. (49) Furthermore, the ability of muscle vibration to entrain firing of these neurons in all treatment groups as they do in Apc^{WT}+control rats further refutes the existence of degeneration’s necessity in signaling disorders (Fig. S21). Overall, our findings suggest that the structure and core ability of mechanosensory neurons to produce action potentials remain unimpaired by codependent neuropathy and does not depend on dying-back degeneration.

Dysfunction depends cancer-chemotherapy interaction

Data presented in Figure 5 suggests damaging cancer-chemotherapy interactions are conserved *in vivo* and have consequences in sensory function. In order to assess the extent of interaction quantitatively, we took an unbiased statistical approach by subjecting all neurons (n=60, 240 total trials) from all experimental groups to a machine learning algorithm (linear discriminant (LD) analysis). Our approach reduced complex feature space into canonical variables giving us a high-level understanding of where interaction emerges, without biased feature selection *a priori*. Our analysis yielded three canonical variables (Fig. 6a) that achieved overall 94.7% classification accuracy (Fig. S19a). We then visualized neuronal signaling in the new 3D composite space created by LD1–3 (Fig. 6a). By projecting high dimensional parameter and feature data onto a simplified 3D canonical space, statistically significant non-linear interaction between cancer and chemotherapy clearly emerged in the first dimension (LD1; 54.23% proportion of variance; Fig. 6a and Fig. S19b). Notably, dysfunction in LD1 induced by the cancer—chemotherapy interaction occurred in the opposite direction to that predicted by independent effects, and its magnitude was amplified greater than their sum (Fig. 6a and Fig. S19b, c). To test the statistical significance of the

cancer—chemotherapy interaction, we conducted Bayesian model comparison with full factorial and all restricted models using leave-one-out cross validation. We then quantified and validated each model's predictive performance by computing the expected log predictive densities (ELPD; measure of a model's out-of-sample predictive accuracy in Fig. 6b–e). We found decisive evidence in favor of a model including a cancer–chemotherapy interaction predictor (ELPD diff ≥ 48 SE <8.1; Fig. 6e). Moreover, our data and generative modeling conclude that codependent interaction (Fig. 6b–d) is necessary to accurately and reliability reproduce clinically relevant neuronal signaling deficits observed in $Apc^{Pirc/+}$+OX rats (Fig. 6e)

Having determined the significance of an interactive effect, we then asked which functional clusters are highly enriched in LD1. By examining the discriminant function coefficients, we found that static signaling and sensitivity functional clusters represent a large portion of the explained variance in LD1. These findings suggest the sensitivity and static signaling clusters are most susceptible to codependent neuropathy (Fig. S19d).

While dynamic signaling provided relatively modest contributions to LD1 (lower coefficient weights in Fig. S19d), examining the parameter level data allowed us to discover the expression of distinct classes of interactions. Independently, OX and $Apc^{Pirc/+}$ induce highly conserved (87.5%) opposing effects exclusively within the dynamic functional cluster. We consistently found that $Apc^{Pirc/+}$ mutation increased and OX treatment decreased dynamic firing (Fig. 6g). This led us to predict that their combination would nullify dysfunction and approximate Apc^{WT}+control signaling. Instead, we observed opposing interactions that resulted in drastic reduction in dynamic firing properties. By contrast, for history-dependent functional clusters, we found that cancer–chemotherapy interaction emerged exclusively in $Apc^{Pirc/+}$+OX neurons, since neither Apc^{WT}+OX nor $Apc^{Pirc/+}$+control neurons were disrupted (Fig. 6h).

Taken together, we found that 58% of the neuronal signaling parameters in $Apc^{Pirc/+}$+OX rats showed high-confidence interaction effects, in that those deficits were greater than those observed in either Apc^{WT}+OX nor $Apc^{Pirc/+}$+control rats. Our findings demonstrate that complex systemic perturbations of chemotherapy and cancer result in synergistic interactions for sensitivity signaling characteristics (Fig. 6f), opposing interactions for peak firing rate during dynamic signaling (Fig. 6g), and emergent interactions for history dependent and static signaling characteristics (Fig. 6h). In summary, $Apc^{Pirc/+}$+OX rats express widespread neuronal signaling dysfunction that targets all functional clusters, was independent of structural or physiologically detected degeneration and were not fully accounted for by a global decrease in sensitivity.

Behavioral dysfunction exacerbated by cancer-chemotherapy interaction

Apc^{WT}+control and $Apc^{Pirc/+}$+control rats achieved a high incidence of rear and fore foot placement, when walking on the rungs of an uneven horizontal ladder, with a foot-drop error rate of only 2.4% (±2.7% SD, 6 animals; Fig. 7a and Movie S1) and 2.5% respectively (±2.9% SD, 4 animals; Figure 7a and Movie S2). In contrast, $Apc^{Pirc/+}$+ OX exhibited a 19.2% foot-drop error rate (±5.6% SD, 7 animals; hierarchical Bayesian model (stan_glm) vs. Apc^{WT}+control and $Apc^{Pirc/+}$+control; Figure 7a and Movie S3). $Apc^{Pirc/+}$+ OX error

rates significantly exceeded our previous findings following OX treatment alone (*Wistar* +OX) of 8.4% (±3.1% SD, 7 animals; hierarchical Bayesian model (stan_glm) vs $Apc^{Pirc/+}$+OX; Figure 7). Independent analysis of fore- Figure 7b, d) and hind-foot (Figure 7c, e) error rates revealed that skilled motor behavior degradation was significantly exacerbated by the emergence of fore-limb errors (10.4%±3.9SD) not present in Apc^{WT}+control (0%), $Apc^{Pirc/+}$+control (2.3%±2.8SD), or *Wistar*+OX (0%; hierarchical Bayesian model (stan_glm)).

Discussion

Here we present original evidence that cancer transforms the nature and magnitude of neuropathy induced by chemotherapy alone. Our preclinical study of rats is the first to compare the neuropathic effects of chemotherapy and cancer, both independently and in combination, currently impractical in human study. These comparisons for global transcriptional analysis of sensory neurons in dorsal root ganglia revealed dysregulation of genes uniquely induced, amplified or suppressed by the combination of cancer and chemotherapy. Codependence was conserved as impaired spike encoding of mechanosensory stimuli and novel ion channelopathy. While the present report is limited to rats, extensive conservation of core molecular and cellular processes across mammalian species (63) leads reasonable expectation that cancer-chemotherapy codependency, whether different in detail, extends to humans. All considered, we conclude that inattention to co-dependencies necessarily prevents the development of mechanism-based treatments for sensory neuropathy, which remains unexplained and unabated in patients receiving chemotherapy for cancer.

Our transcription analyses expose two potential targets for treating sensorimotor disorders among the debilitating patient symptoms that persist following treatment of various cancers with platinum-based compounds and other antineoplastic agents, e.g. taxanes. Patients display deficits in the spatiotemporal parameters (speed and stride) of walking gait, in control of posture, and in balance relying on proprioception (64). Acknowledging that these disabilities may arise from a variety of lesions in the nervous system, the deficits we observe here at the receptor origin of detection and encoding of muscle mechanics would necessarily impair movements and postures and cannot be fully compensated by other senses, e.g. vision. Furthermore, signaling by mechanosensory neurons in rats closely resembles that in human (62). For these reasons, we assign special attention to depressed signaling by muscle spindles and to the associated decrease in expression of the voltage-gated ion channel Kv3.3 and its gene *Kcnc3*. Reports that *Kcnc3* gene knock out impairs firing responses of neurons and results in ataxia (61) promote this gene and its ion channel as potential contributors to signaling deficits observed in the present study. At this time, we are uncertain about the sufficiency of Kv3.3 channelopathy to explain deficient mechanosensory signaling in cancer treated by chemotherapy. Uncertainty arises in part, because comprehensive understanding of the molecular mechanisms underlying the function of these sensory neurons is lacking, although advanced by our discovery of Kv3.3 in mechanoreceptors of healthy animals. Another candidate target for treating sensorimotor disorders is the inflammatory signaling molecule IL6, shown here to express large increases in both gene and protein expression. As a result of its effect in suppressing neuronal firing behavior (51) IL6 has the potential to

explain decreased signaling by mechanosensory neurons. We identify both Kv3.3 and IL6, therefore, as targets worthy of testing for their potential value in treating movement disorders. Additional points of interaction likely exist, which remain either undiscussed (e.g. FosB) or potentially masked due to transcriptional profiling of DRG's that may result in variable differential expression across heterogenous cell types (Fig. 1d).

We observed abnormal skilled sensorimotor behavior in $Apc^{Pirc/+}$+OX rats. Deficits were significantly greater than those previously observed in our lab from animals treated with OX alone (23). The emergence of novel forelimb deficits typically not observed in this challenge to hindlimb capacities provides further evidence that exacerbation effects are unpredicted from studying chemotherapy alone. Further our data indicates that intact proprioceptive sensory input from muscle spindles is necessary to ensure limb placement accuracy in a skilled behavioral task and may be sufficient to explain sensorimotor deficits experienced by cancer survivors.

Our study, being restricted to a single time point following chemotherapy, does not assess the stability of potential treatment targets that emerge from codependent neuropathy. It is reasonable to expect, however, that the codependence undergoes dynamic change. Cancer, presumably also its associated systemic effects, undergoes complex progression as subpopulations of cancer cells differentially resist, adapt, or succumb to chemotherapy. Similarly, surgical resection of tumors or surgical associated analgesics might impose additional points of interaction that have the potential to impact DRG neurobiology. Moreover, biological systems themselves initiate dynamic responses to perturbations. In the nervous system, homeostatic regulation initiates compensatory mechanisms to offset perturbations in neuronal excitability (59). It is thought provoking in this regard to consider the possibility that the chronic hypoexcitability which follows the acute hyperexcitability (2, 19) that develops during chemotherapy reflects the actions of a dysregulated compensatory mechanism. Understanding these non-linear interactions processes and their effects on potential treatment are both challenging and necessary for developing effective cancer treatment.

Supplementary Material

Refer to Web version on PubMed Central for supplementary material.

Acknowledgements:

This work is supported by NIH grant R01CA221363 and R01HD090642. We thank staff of the Physiological Research Laboratory at Georgia Institute of Technology. We are grateful to Dr. Thomas Burkholder for technical assistance, discussions and comments. We thank Dr. Mengnan Zhang and Dr. Evan Clayton for discussions and comments.

References

1. André T, Boni C, Mounedji-Boudiaf L, Navarro M, Tabernero J, Hickish T, Topham C, Zaninelli M, Clingan P, Bridgewater J. Oxaliplatin, fluorouracil, and leucovorin as adjuvant treatment for colon cancer. New England Journal of Medicine. 2004;350(23):2343–51. [PubMed: 15175436]
2. Cavaletti G, Marmiroli P. Chemotherapy-induced peripheral neurotoxicity. Nature Reviews Neurology. 2010;6(12):657. [PubMed: 21060341]

3. Alcindor T, Beauger N. Oxaliplatin: a review in the era of molecularly targeted therapy. Current oncology. 2011;18(1):18. [PubMed: 21331278]
4. Seretny M, Currie GL, Sena ES, Ramnarine S, Grant R, MacLeod MR, Colvin LA, Fallon M. Incidence, prevalence, and predictors of chemotherapy-induced peripheral neuropathy: a systematic review and meta-analysis. PAIN®. 2014;155(12):2461–70. [PubMed: 25261162]
5. Sisignano M, Baron R, Scholich K, Geisslinger G. Mechanism-based treatment for chemotherapy-induced peripheral neuropathic pain. Nat Rev Neurol. 2014;10(12):694–707. Epub 2014/11/05. doi: 10.1038/nrneurol.2014.211. [PubMed: 25366108]
6. Avan A, Postma TJ, Ceresa C, Avan A, Cavaletti G, Giovannetti E, Peters GJ. Platinum-induced neurotoxicity and preventive strategies: past, present, and future. The oncologist. 2015:theoncologist 2014–0044.
7. Galanski M, Jakupec MA, Keppler BK. Update of the preclinical situation of anticancer platinum complexes: novel design strategies and innovative analytical approaches. Current medicinal chemistry. 2005;12(18):2075–94. [PubMed: 16101495]
8. Johnstone TC, Park GY, Lippard SJ. Understanding and improving platinum anticancer drugs–phenanthriplatin. Anticancer research. 2014;34(1):471–6. [PubMed: 24403503]
9. Hershman DL, Lacchetti C, Dworkin RH, Lavoie Smith EM, Bleeker J, Cavaletti G, Chauhan C, Gavin P, Lavino A, Lustberg MB. Prevention and management of chemotherapy-induced peripheral neuropathy in survivors of adult cancers: American Society of Clinical Oncology clinical practice guideline. Journal of Clinical Oncology. 2014;32(18):1941–67. [PubMed: 24733808]
10. Currie GL, Angel-Scott H, Colvin L, Cramond F, Hair K, Khandoker L, Liao J, Macleod MR, McCann SK, Morland R. Animal models of chemotherapy-induced peripheral neuropathy: a machine-assisted systematic review and meta-analysis A comprehensive summary of the field to inform robust experimental design. bioRxiv. 2018:293480.
11. Boyette-Davis JA, Eng C, Wang XS, Cleeland CS, Wendelschafer-Crabb G, Kennedy WR, Simone DA, Zhang H, Dougherty PM. Subclinical peripheral neuropathy is a common finding in colorectal cancer patients prior to chemotherapy. Clinical Cancer Research. 2012;18(11):3180–7. [PubMed: 22496202]
12. Ahles TA. Brain vulnerability to chemotherapy toxicities. Psycho-Oncology. 2012;21(11):1141–8. [PubMed: 23023994]
13. Reuter S, Gupta SC, Chaturvedi MM, Aggarwal BB. Oxidative stress, inflammation, and cancer: how are they linked? Free Radical Biology and Medicine. 2010;49(11):1603–16. [PubMed: 20840865]
14. Zheng Q, Fang D, Cai J, Wan Y, Han J-S, Xing G-G. Enhanced excitability of small dorsal root ganglion neurons in rats with bone cancer pain. Molecular pain. 2012;8(1):24. [PubMed: 22472208]
15. Amos-Landgraf JM, Kwong LN, Kendziorski CM, Reichelderfer M, Torrealba J, Weichert J, Haag JD, Chen K-S, Waller JL, Gould MN. A target-selected Apc-mutant rat kindred enhances the modeling of familial human colon cancer. Proceedings of the National Academy of Sciences. 2007;104(10):4036–41.
16. Irving AA, Yoshimi K, Hart ML, Parker T, Clipson L, Ford MR, Kuramoto T, Dove WF, Amos-Landgraf JM. The utility of Apc-mutant rats in modeling human colon cancer. Disease models & mechanisms. 2014;7(11):1215–25. [PubMed: 25288683]
17. Washington MK, Powell AE, Sullivan R, Sundberg JP, Wright N, Coffey RJ, Dove WF. Pathology of rodent models of intestinal cancer: progress report and recommendations. Gastroenterology. 2013;144(4):705–17. [PubMed: 23415801]
18. Reagan-Shaw S, Nihal M, Ahmad N. Dose translation from animal to human studies revisited. The FASEB journal. 2008;22(3):659–61. [PubMed: 17942826]
19. Park SB, Goldstein D, Krishnan AV, Lin CSY, Friedlander ML, Cassidy J, Koltzenburg M, Kiernan MC. Chemotherapy-induced peripheral neurotoxicity: A critical analysis. CA: a cancer journal for clinicians. 2013;63(6):419–37. [PubMed: 24590861]
20. Grisold W, Cavaletti G, Windebank AJ. Peripheral neuropathies from chemotherapeutics and targeted agents: diagnosis, treatment, and prevention. Neuro-oncology. 2012;14(suppl_4):iv45–iv54. [PubMed: 23095830]

21. Cavaletti G, Tredici G, Petruccioli M, Donde E, Tredici P, Marmiroli P, Minoia C, Ronchi A, Bayssas M, Etienne GG. Effects of different schedules of oxaliplatin treatment on the peripheral nervous system of the rat. European journal of cancer. 2001;37(18):2457–63. [PubMed: 11720843]
22. Nardelli P, Powers R, Cope TC, Rich MM. Increasing motor neuron excitability to treat weakness in sepsis. Annals of neurology. 2017;82(6):961–71. [PubMed: 29171917]
23. Vincent JA, Wieczerzak KB, Gabriel HM, Nardelli P, Rich MM, Cope TC. A novel path to chronic proprioceptive disability with oxaliplatin: distortion of sensory encoding. Neurobiology of disease. 2016;95:54–65. [PubMed: 27397106]
24. Vincent JA, Gabriel HM, Deardorff AS, Nardelli P, Fyffe RE, Burkholder T, Cope TC. Muscle proprioceptors in adult rat: mechanosensory signaling and synapse distribution in spinal cord. Journal of neurophysiology. 2017;118(5):2687–701. [PubMed: 28814636]
25. Carrasco DI, Vincent JA, Cope TC. Distribution of TTX-sensitive voltage-gated sodium channels in primary sensory endings of mammalian muscle spindles. Journal of Neurophysiology. 2017;117(4):1690–701. [PubMed: 28123009]
26. Lili LN, Matyunina LV, Walker L, Benigno BB, McDonald JF. Molecular profiling predicts the existence of two functionally distinct classes of ovarian cancer stroma. BioMed research international. 2013;2013.
27. Smyth GK. Linear models and empirical bayes methods for assessing differential expression in microarray experiments. Statistical applications in genetics and molecular biology. 2004;3(1):1–25.
28. Ritchie ME, Silver J, Oshlack A, Holmes M, Diyagama D, Holloway A, Smyth GK. A comparison of background correction methods for two-colour microarrays. Bioinformatics. 2007;23(20):2700–7. [PubMed: 17720982]
29. Husson F, Josse J, Pages J. Principal component methods-hierarchical clustering-partitional clustering: why would we need to choose for visualizing data. Applied Mathematics Department. 2010.
30. Argüelles M, Benavides C, Fernández I. A new approach to the identification of regional clusters: hierarchical clustering on principal components. Applied Economics. 2014;46(21):2511–9.
31. Kassambara A, Mundt F. Factoextra: extract and visualize the results of multivariate data analyses. R package version. 2016;1(3).
32. Warnes MGR, Bolker B, Bonebakker L, Gentleman R. Package 'gplots'. Various R Programming Tools for Plotting Data. 2016.
33. Murtagh F, Legendre P. Ward's hierarchical agglomerative clustering method: which algorithms implement Ward's criterion? Journal of classification. 2014;31(3):274–95.
34. Becker R, Chambers J, Wilks A. The New S Language Pacific Grove CA: Wadsworth & Brooks/Cole. BeckerThe New S Language1988. 1988.
35. Huang DW, Sherman BT, Lempicki RA. Systematic and integrative analysis of large gene lists using DAVID bioinformatics resources. Nature protocols. 2008;4(1):44.
36. Hong G, Zhang W, Li H, Shen X, Guo Z. Separate enrichment analysis of pathways for up-and downregulated genes. Journal of the Royal Society Interface. 2014;11(92):20130950.
37. Woo S-H, Lukacs V, De Nooij JC, Zaytseva D, Criddle CR, Francisco A, Jessell TM, Wilkinson KA, Patapoutian A. Piezo2 is the principal mechanotransduction channel for proprioception. Nature neuroscience. 2015;18(12):1756. [PubMed: 26551544]
38. Simon A, Shenton F, Hunter I, Banks RW, Bewick GS. Amiloride-sensitive channels are a major contributor to mechanotransduction in mammalian muscle spindles. The Journal of physiology. 2010;588(1):171–85. [PubMed: 19917568]
39. de Nooij JC, Simon CM, Simon A, Doobar S, Steel KP, Banks RW, Mentis GZ, Bewick GS, Jessell TM. The PDZ-domain protein Whirlin facilitates mechanosensory signaling in mammalian proprioceptors. Journal of Neuroscience. 2015;35(7):3073–84. [PubMed: 25698744]
40. Bewick GS, Banks RW. Mechanotransduction in the muscle spindle. Pflügers Archiv-European Journal of Physiology. 2015;467(1):175–90. [PubMed: 24888691]
41. Gabry J, Goodrich B. rstanarm: Bayesian applied regression modeling via Stan. R package version. 2018;218.1.

42. Brooks S, Gelman A, Jones G, Meng X-L. Handbook of markov chain monte carlo: CRC press; 2011.
43. Hoffman MD, Gelman A. The No-U-turn sampler: adaptively setting path lengths in Hamiltonian Monte Carlo. Journal of Machine Learning Research. 2014;15(1):1593–623.
44. Gelman A, Rubin DB. Inference from iterative simulation using multiple sequences. Statistical science. 1992;7(4):457–72.
45. Metz GA, Whishaw IQ. The ladder rung walking task: a scoring system and its practical application. JoVE (Journal of Visualized Experiments). 2009(28):e1204.
46. Kwong LN, Dove WF. APC and its modifiers in colon cancer. APC Proteins: Springer; 2009 p. 85–106.
47. DeBerardinis RJ, Lum JJ, Hatzivassiliou G, Thompson CB. The biology of cancer: metabolic reprogramming fuels cell growth and proliferation. Cell metabolism. 2008;7(1):11–20. [PubMed: 18177721]
48. Hay N Reprogramming glucose metabolism in cancer: can it be exploited for cancer therapy? Nature Reviews Cancer. 2016;16(10):635. [PubMed: 27634447]
49. Burakgazi A, Messersmith W, Vaidya D, Hauer P, Hoke A, Polydefkis M. Longitudinal assessment of oxaliplatin-induced neuropathy. Neurology. 2011;77(10):980–6. [PubMed: 21865571]
50. Vezzani A, Viviani B. Neuromodulatory properties of inflammatory cytokines and their impact on neuronal excitability. Neuropharmacology. 2015;96:70–82. [PubMed: 25445483]
51. Nelson TE, Ur CL, Gruol DL. Chronic interleukin-6 exposure alters electrophysiological properties and calcium signaling in developing cerebellar purkinje neurons in culture. Journal of neurophysiology. 2002;88(1):475–86. [PubMed: 12091569]
52. Sittl R, Lampert A, Huth T, Schuy ET, Link AS, Fleckenstein J, Alzheimer C, Grafe P, Carr RW. Anticancer drug oxaliplatin induces acute cooling-aggravated neuropathy via sodium channel subtype Na(V)1.6-resurgent and persistent current. Proc Natl Acad Sci U S A. 2012;109(17):6704–9. Epub 2012/04/12. doi: 10.1073/pnas.1118058109. [PubMed: 22493249]
53. Ahles TA, Saykin AJ. Candidate mechanisms for chemotherapy-induced cognitive changes. Nature Reviews Cancer. 2007;7(3):192. [PubMed: 17318212]
54. Argyriou AA, Bruna J, Genazzani AA, Cavaletti G. Chemotherapy-induced peripheral neurotoxicity: management informed by pharmacogenetics. Nature Reviews Neurology. 2017;13(8):492. [PubMed: 28664909]
55. Chalfie M Neurosensory mechanotransduction. Nature reviews Molecular cell biology. 2009;10(1):44. [PubMed: 19197331]
56. Maksimovic S, Nakatani M, Baba Y, Nelson AM, Marshall KL, Wellnitz SA, Firozi P, Woo S-H, Ranade S, Patapoutian A. Epidermal Merkel cells are mechanosensory cells that tune mammalian touch receptors. Nature. 2014;509(7502):617. [PubMed: 24717432]
57. Proske U, Gandevia SC. The kinaesthetic senses. The Journal of physiology. 2009;587(17):4139–46. [PubMed: 19581378]
58. Rudy B, Chow A, Lau D, Amarillo Y, Ozaita A, Saganich M, Moreno H, Nadal MS, HERNANDEZ-PINEDA R, HERNANDEZ-CRUZ A. Contributions of Kv3 channels to neuronal excitability. Annals of the New York Academy of Sciences. 1999;868(1):304–43. [PubMed: 10414303]
59. Waxman SG, Zamponi GW. Regulating excitability of peripheral afferents: emerging ion channel targets. Nature neuroscience. 2014;17(2):153. [PubMed: 24473263]
60. Akemann W, Knöpfel T. Interaction of Kv3 potassium channels and resurgent sodium current influences the rate of spontaneous firing of Purkinje neurons. Journal of Neuroscience. 2006;26(17):4602–12. [PubMed: 16641240]
61. Figueroa KP, Minassian NA, Stevanin G, Waters M, Garibyan V, Forlani S, Strzelczyk A, Bürk K, Brice A, Dürr A. KCNC3: phenotype, mutations, channel biophysics—a study of 260 familial ataxia patients. Human mutation. 2010;31(2):191–6. [PubMed: 19953606]
62. Burke D, Hagbarth K-E, Löfstedt L. Muscle spindle activity in man during shortening and lengthening contractions. The Journal of physiology. 1978;277(1):131–42. [PubMed: 148511]
63. Breschi A, Gingeras TR, Guigó R. Comparative transcriptomics in human and mouse. Nature Reviews Genetics. 2017;18(7):425.

64. Marshall TF, Zipp GP, Battaglia F, Moss R, Bryan S. Chemotherapy-induced-peripheral neuropathy, gait and fall risk in older adults following cancer treatment. Journal of Cancer Research and Practice. 2017.

Statement of Significance:

Findings highlight the need to account for pathobiological interactions between cancer and chemotherapy as a major contributor to neuropathy and will have significant and immediate impact on future investigations in this field.

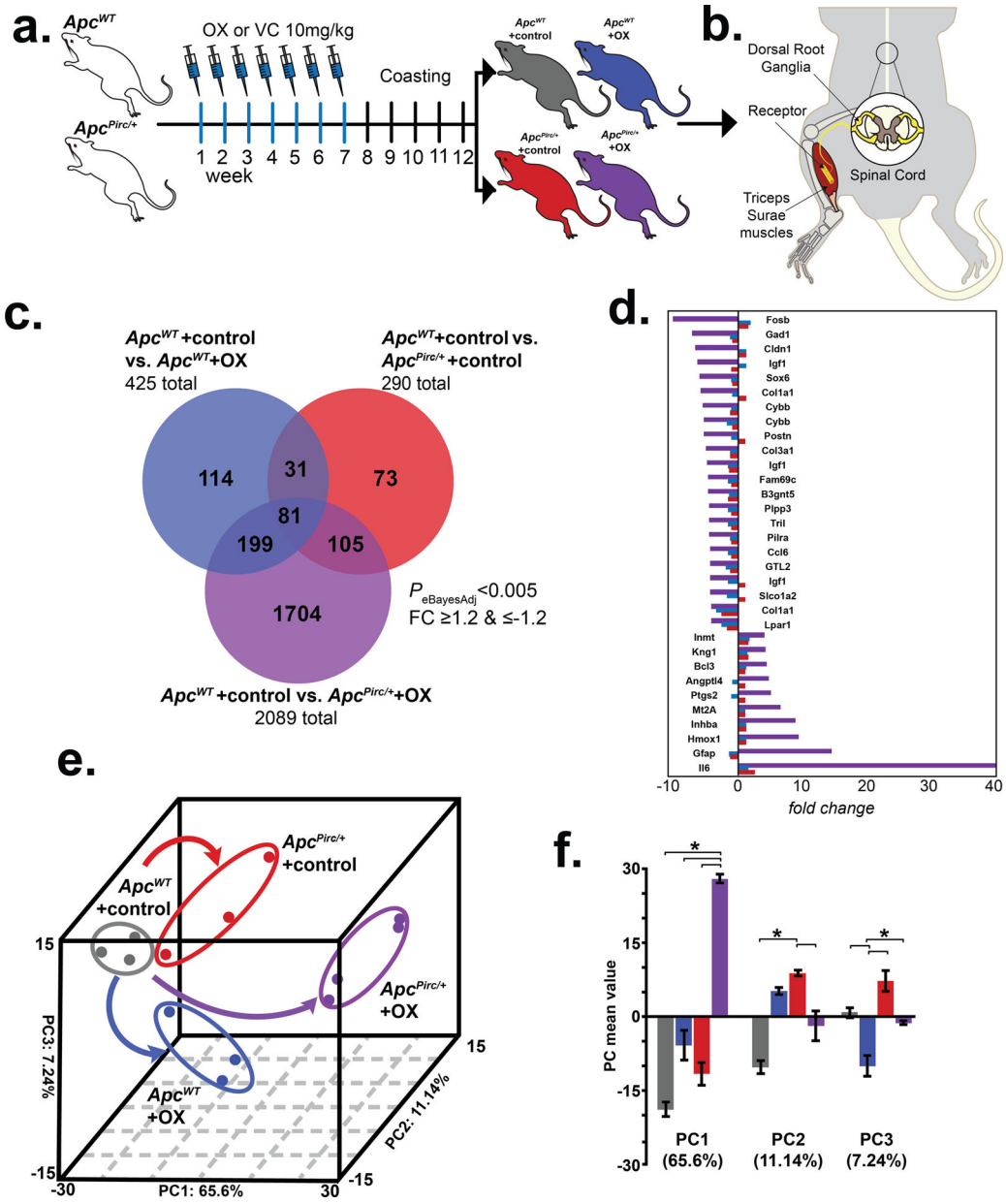

Figure 1. Cancer-chemotherapy codependence amplifies transcriptional dysregulation.

a, Schematic of treatment schedule of oxaliplatin (OX) and vehicle control (VC) generating four independent experimental groups in wild-type (Apc^{WT}) and autosomal dominant mutation of the adenomatous polyposis coli gene ($Apc^{Pirc/+}$): Apc^{WT}+control, Apc^{WT}+OX, $Apc^{Pirc/+}$+control, and $Apc^{Pirc/+}$+OX rats. **b**, Diagram of experimental targets of lumbosacral dorsal root ganglia (DRG) and muscle for assaying transcriptomes and/or cell-specific protein expression in rat models. **c**, Venn-diagram distribution of significantly differentially expressed genes from the lumbosacral DRG among all groupwise contrasts. Significance determined by both $P < 0.005$ and fold-change (FC) ≥ 1.2 and ≤ −1.2 using a Bayesian moderated linear fixed effects model ($eBayes_{Adj}$). **d**, Bar graphs outline the top differentially expressed genes in $Apc^{Pirc/+}$+OX (purple bars) animals (FC ≥ 4 and ≤ −4) as

compared to the effects observed in Apc^{WT}+OX (blue bars) or $Apc^{Pirc/+}$+control (red bars). **e**, Group correlation determined by principal-component (PC) analysis of significantly differentially expressed genes. Genes were visualized in the new 3D composite space created by PC1–3. Effects of independent chemotherapy (Apc^{WT}+OX) or cancer ($Apc^{Pirc/+}$+control) and their combinatorial ($Apc^{Pirc/+}$+OX) treatment are indicated by curved arrows; dots represent individual animals. **f**, Bar graphs of the mean values of PC1, PC2, and PC3. Error bars represent s.e.m. * indicates statistically significant differences between experimental groups as empirically derived from hierarchical Bayesian model (stan_glm).

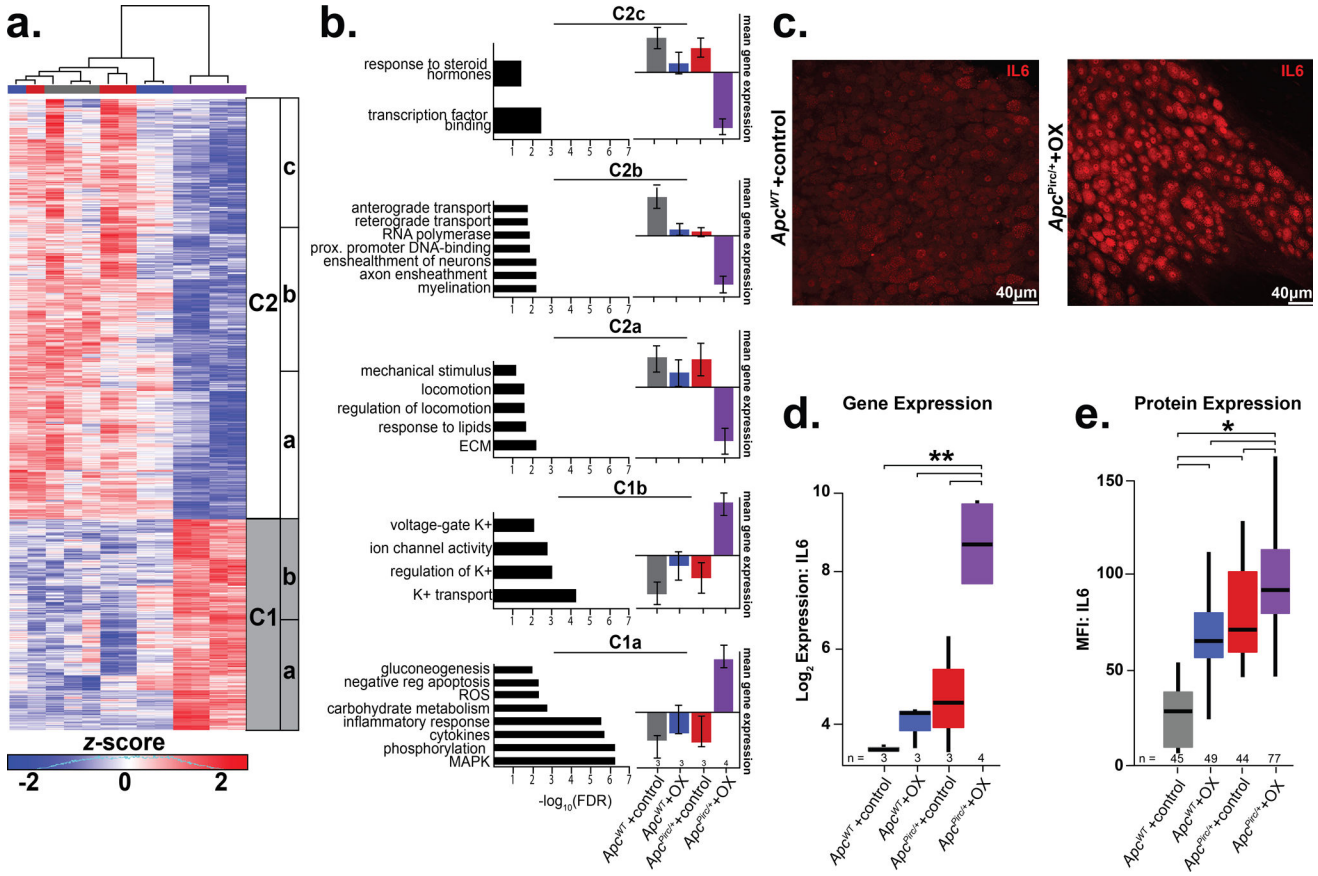

Figure 2. Cancer-chemotherapy interaction disrupts distinct biological processes.

a, Heatmap of the top differentially expressed genes in the sensory neurons identified by PC1 driven hierarchical-clustering (biological triplicates n= 3 for Apc^{WT}+control, , Apc^{WT} +OX, $Apc^{Pirc/+}$+control and four biologic replicates for $Apc^{Pirc/+}$+OX). Data were mean-centered and s.d. normalized before clustering; upregulated and downregulated genes (row) are shown in red and blue, respectively. Grey and white bars (C1 and C2 respectively) display the main clusters from gene level hierarchical-clustering and were chosen for clarity, while subclusters (**a-c**) highlight unique biologic characteristics within the main clusters. **b**, Clusters showing distinct up- or downregulation of key biological processes (Gene Ontology (GO) terms) and pathways (Kyoto Encyclopedia of Genes and Genomes (KEGG)). Selected pathway and gene ontology terms significantly associated (false discovery rate [FDR] ≤ 0.25) with misregulated transcripts in individual clusters are listed on the left of each gene cluster with significance indicated by horizontal bars ($-\log_{10}$(FDR)). The vertical bar graphs on the right compare mean ± s.d. of gene expression levels in each sub-cluster (Table S1). **c**, Confocal images of DRGs from Apc^{WT}+control and $Apc^{Pirc/+}$+OX imminostained against interleukin 6 (IL6). Scale bar, 40 μm. Gene expression (**d**) and receptor protein expression (**e**, mean fluorescence intensity (MFI)) of IL6 as determined by transcriptional profiling and cell-specific immunohistochemistry of large diameter sensory neurons (> 30μm). Numbers (n) identify sample size for each group. * indicates statistically significant differences between experimental groups as empirically derived from hierarchical Bayesian model

(stan_glm). ** indicates $eBayes_{Adj} < 0.005$ and fold-change (FC) ≥ 1.2 and ≤ −1.2 using a Bayesian moderated linear fixed effects model. Data presented as mean ± s.d.

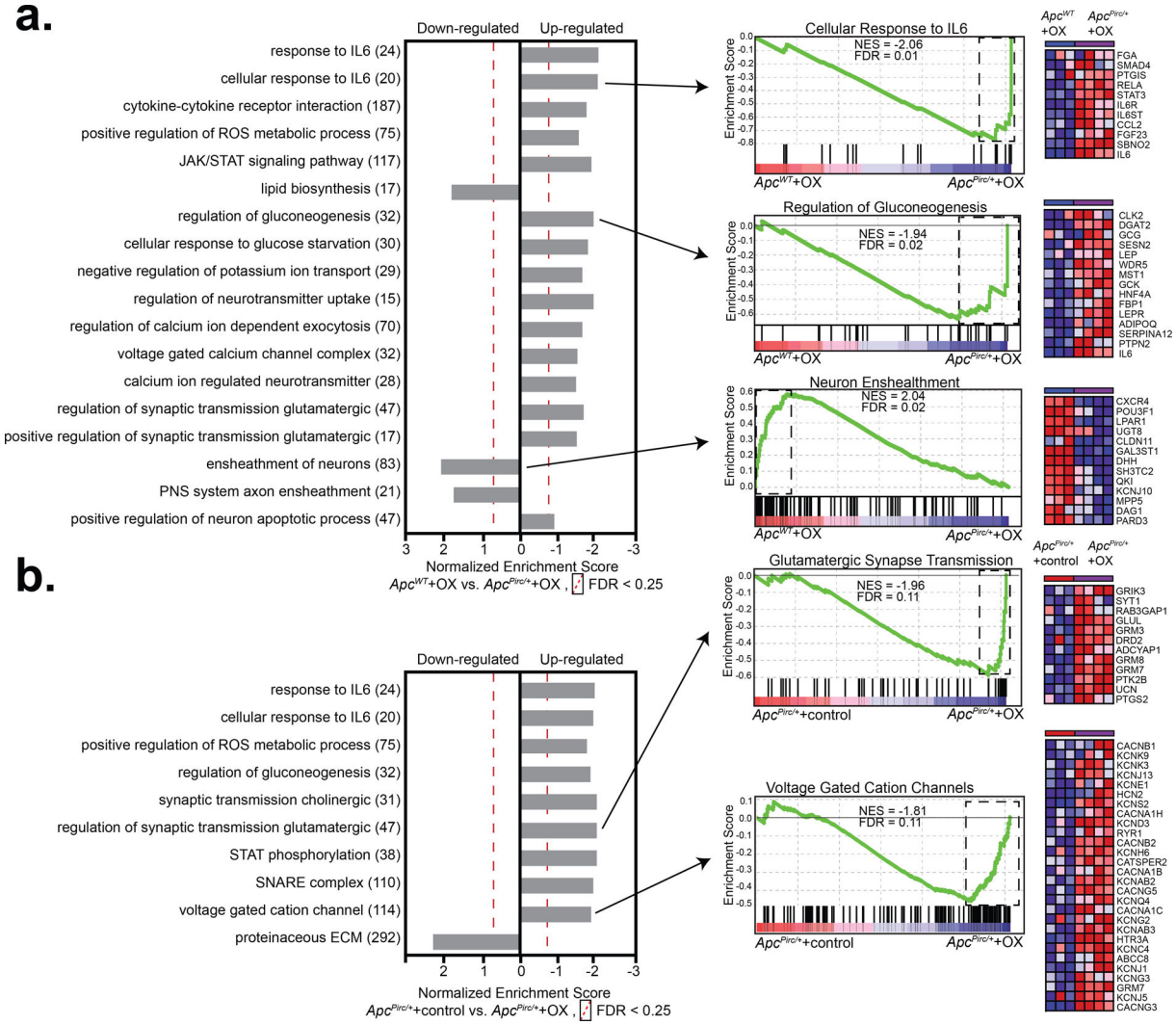

Figure 3. GSEA and pathway analyses test codependence of cancer and chemotherapy.

Enriched gene sets in sensory neurons identified by gene set enrichment analysis (GSEA: MSigDB, C2-CP: canonical pathways; C3- MIR: microRNA targets; C3- TFT: transcription factor targets; C5-BP: GO biological process; C5- CC: GO cellular component; C5- MF: GO molecular function C7: immunologic signatures gene sets from the comparison of **a**, , *Apc*^{WT}+OX and *Apc*$^{Pirc/+}$+OX and **b**, *Apc*$^{Pirc/+}$+control and *Apc*$^{Pirc/+}$+OX groups. Individual frames (horizontal grey bars) identify functionally related (internally consistent) groups of gene sets expressing distinct up- or downregulation as compared with *Apc*^{WT} +OX. Number of overlapping genes displayed in parentheses to the right of the corresponding GO term. Representative enrichment plots are shown in the middle column. Heat-map representation of leading-edge genes is shown on right. Statistical significance determined by permutation testing with normalized enrichment score (NES) and Benjamini–Hochberg false discovery rate (FDR) < 0.25. DEG, differentially expressed genes; ROS, reactive oxygen species: ECM, extracellular matrix

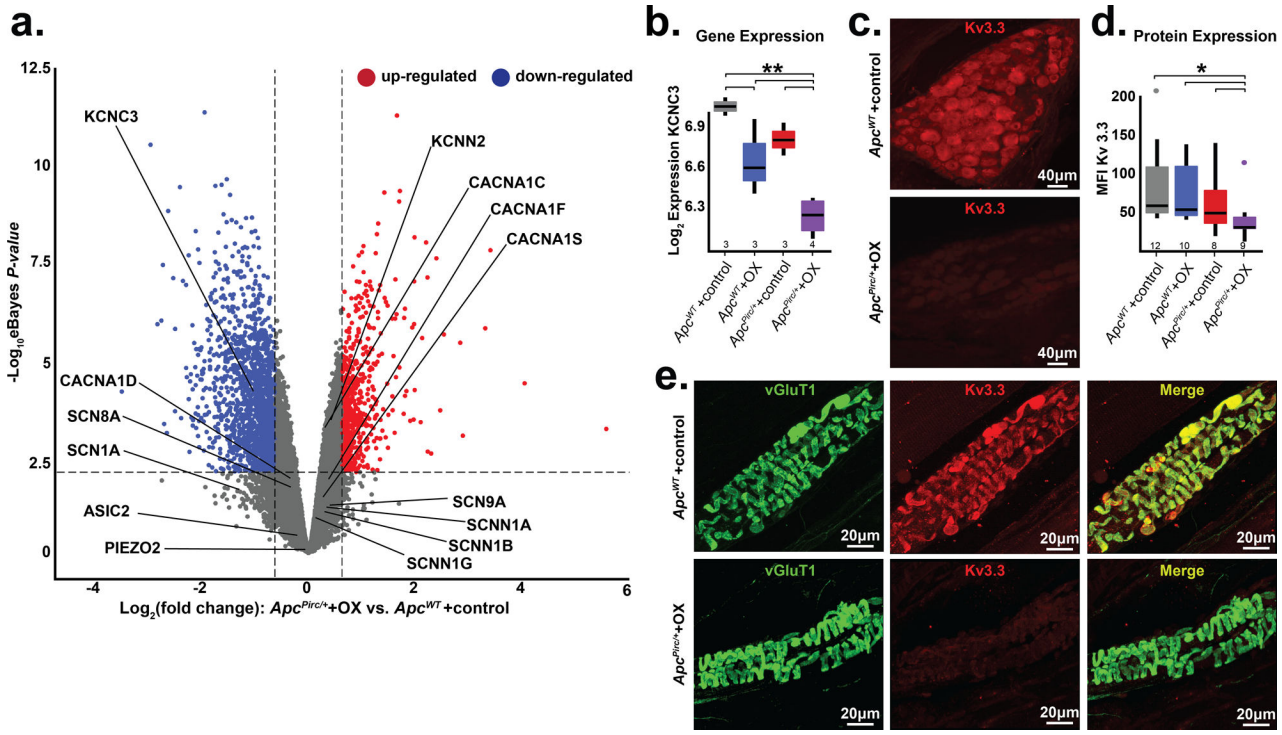

Figure 4. Targeted transcriptional analysis reveals mechanisms for cancer-chemotherapy interaction.

a, Volcano plot comparing up- and downregulated genes in *Apc*$^{Pirc/+}$+OX and *Apc*^{WT} +control sensory neuron transcriptomes. Annotation of genes involved in mechanotransduction, signal amplification, action potential generation and maintenance is shown. Significance was determined as Benjamini–Hochberg FDR < 0.01 and $\log_2$fold change ≥ 1. **b**, Gene expression of Kcnc3 encoding Kv3.3, as determined through transcriptional profiling (Kcnc3: 1369133_a_at). **c**, Confocal images of dorsal root ganglia immunolabeled against Kv3.3 illustrates expression of *Apc*$^{Pirc/+}$+OX relative to *Apc*^{WT} +control neurons. **d**, Quantification of receptor protein expression (mean fluorescence intensity (MFI)) of Kv3.3 determined through averaging over all annulospiral endings (617 from 12 *Apc*^{WT}+control neurons, 434 from 10 *Apc*^{WT}+OX neurons, 459 from 8 *Apc*$^{Pirc/+}$ +control neurons, and 362 from 9 *Apc*$^{Pirc/+}$+OX neurons) for each neuron per experimental group. **e**, Confocal images of mechanosensory nerve terminals in muscle spindles immunolabeled against VGluT1 (green), Kv3.3 (red), and merged (yellow) illustrates protein expression levels and distribution in *Apc*$^{Pirc/+}$+OX relative to *Apc*^{WT}+control. * indicates statistically significant differences between experimental groups as empirically derived from hierarchical Bayesian model (stan_glm). ** indicates $P_{eBayesAdj} < 0.005$ and fold-change (FC) ≥ 1.2 and ≤ −1.2 using a Bayesian moderated linear fixed effects model. Data presented as mean ± s.e.m.

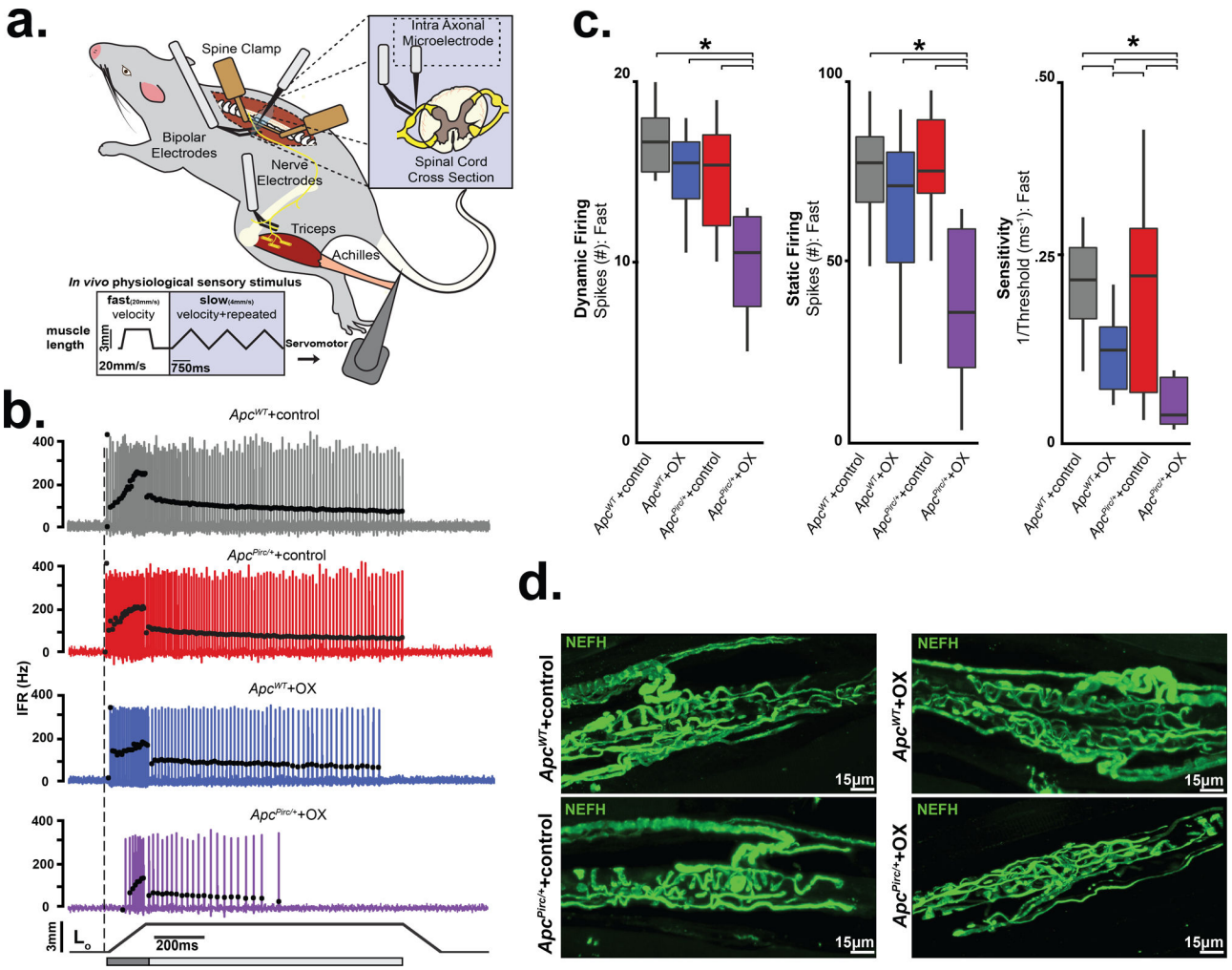

Figure 5. Mechanosensory signal degradation exacerbated by the cancer–chemotherapy interaction.

a, Diagram of anesthetized rat stabilized in spine clamps for physiological recordings of triceps surae (medial and lateral gastrocnemius and soleus) muscles and nerves. Records taken intra-axonally from single mechanosensory neurons in lumbosacral dorsal roots (L4-S1) while applying fast (20 mm/second). **b**, Representative cases of spiking activity in *Apc*^{WT}+control, *Apc*^{WT}+OX, *Apc*$^{Pirc/+}$+control, and *Apc*$^{Pirc/+}$+OX as a measure of sensory encoding. Black circles plot instantaneous firing rates (pps) of corresponding spike (action potential) intervals. Dashed vertical line marks onset of muscle stretch (3mm from resting length (Lo)) shown in bottom trace divided into dynamic and static phases by dark grey (150 ms duration after stretch command onset) and light grey (1 s duration after the dynamic phase) bars. **c**, Neuronal spiking parameters (n=31 averaged from four trials in each neuron, four shown from fast ramp stimulus) representing different features of sensory stimulus (*Apc*^{WT}+control (n = 11), *Apc*^{WT}+OX (n = 19), *Apc*$^{Pirc/+}$+control (n = 20) and *Apc*$^{Pirc/+}$ +OX (n = 10)): mean initial burst frequency (pps) signaling stretch onset; the number of spikes during dynamic sensory stimulation (shown as a dark grey bar in b); the number of spikes during static sensory stimulation (shown as a light grey bar in b); sensitivity assessed as the inverse of latency to stimulus detection (ms-1), i.e. lower sensitivity corresponds to

longer latency and higher threshold. **d**, Confocal image of a neurofilament heavy-chain (NEFH, in green) with immunolabeling of the terminal axon and receptor structure in Apc^{WT}+control, Apc^{WT}+OX, $Apc^{Pirc/+}$+control, and $Apc^{Pirc/+}$+OX rats. Scale bar, 15 μm. * indicates statistically significant differences between experimental groups as empirically derived from hierarchical Bayesian model (stan_glm): 95% highest density intervals do not overlap between groupwise contrasts. Data presented as mean±s.e.m.

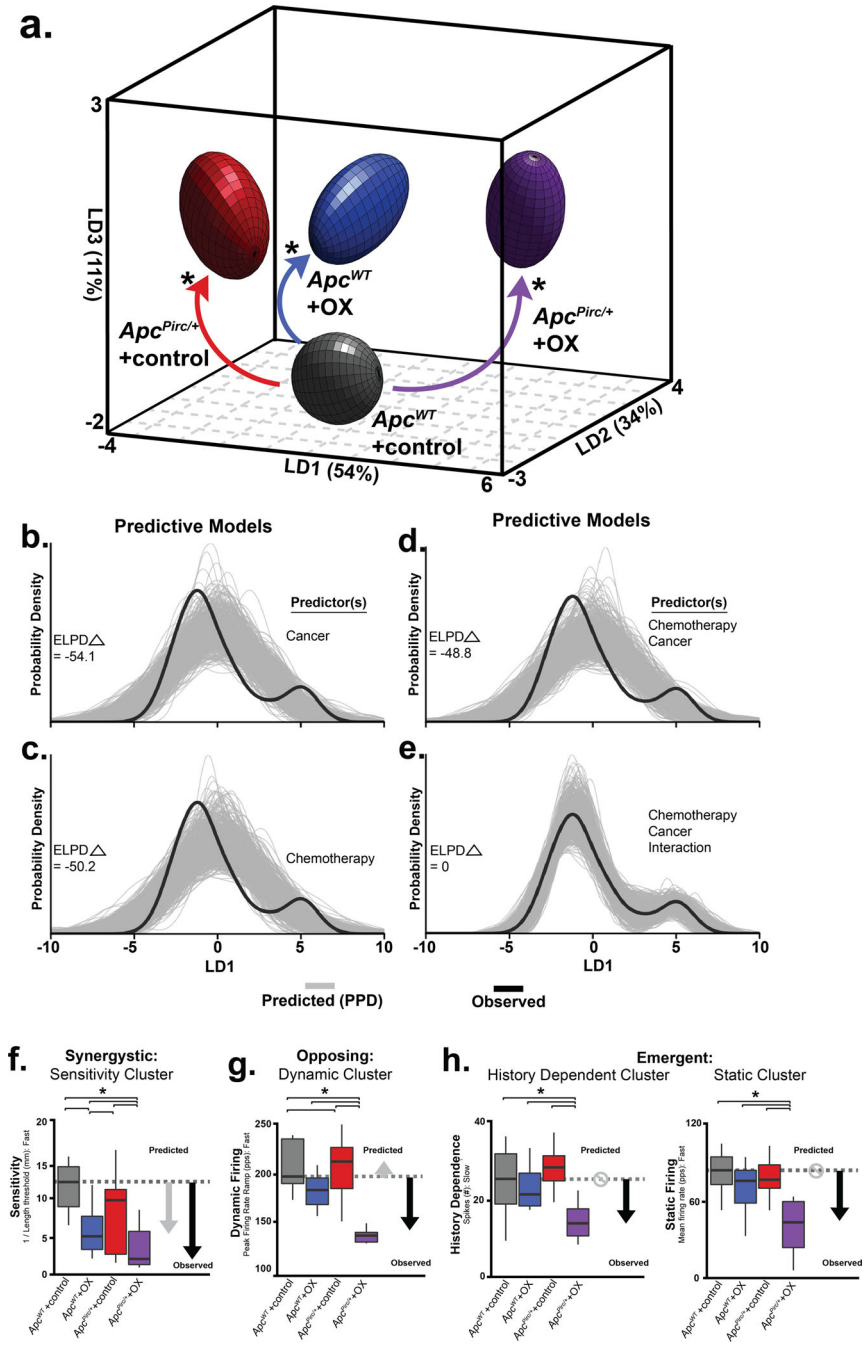

Figure 6. Cancer-chemotherapy codependence exacerbates sensory dysfunction beyond that predicted by cancer or chemotherapy alone.

a, Neuronal spiking parameters (n=31, averaged from four trials, from each neuron (n=60)) representing different features of sensory stimuli were subjected to linear discriminant (LD) analysis. Neuronal signaling was visualized in the new 3D composite space created by LD1–3. 3D ellipsoids enclosing 68% of data were computed with least-squares elliptical fitting to emphasize differences between control and *Apc*$^{Pirc/+}$+OX neurons. Effects of independent (OX or *Apc*$^{Pirc/+}$) and combinatorial (*Apc*$^{Pirc/+}$+OX) treatment are indicated by curved arrows. **b-e**, the hierarchical Bayesian model used to test for significant group differences in

LD1 scores reconfigured to operate in a predictive fashion. Predictors included in each model are listed to the right of each plot. Generative models in (**b-d**) utilizing one (**b, c**) or both independent (**d**) predictor(s), i.e. cancer ($Apc^{Pirc/+}$) or chemotherapy (OX) for posterior prediction. The generative model in (**e**) utilizes both independent predictors and an interaction term for posterior prediction. Grey lines in b-e represent 500 novel (generative) samples drawn from the posterior distributions. Black lines illustrate experimentally observed mean LD1 score. Predictive accuracy was measured by calculating expected log predictive density (ELPD) for each model and benchmarked off of the highest performing model. Delta ELPD (Δ symbol) indicates difference from optimal model. Negative models represent worse predictive performance. **f**, Sensitivity assessed as the inverse of latency to stimulus detection (mm-1), i.e. lower sensitivity corresponds to longer latency and higher threshold. **g**, Peak firing rate (pps) achieved during the dynamic sensory stimulus (shown as dark grey bar in Fig. 5b). **h**, change in dynamic spike number in successive, slow stretch dynamic sensory stimulus and mean firing rate (pps) achieved during the static sensory stimulus (shown as light grey bar in Fig. 5b). Recordings were analyzed from Apc^{WT} +control (n = 11), Apc^{WT}+OX (n = 19), $Apc^{Pirc/+}$+control (n = 20) and $Apc^{Pirc/+}$+OX (n = 10) in **b-g**, * indicates statistically significant differences between experimental groups as empirically derived from hierarchical Bayesian model (stan_glm). Grey arrows in **f-h** indicate direction and significant differences from Apc^{WT}+control predicted from the linear sum of the independent effects of Apc^{WT}+OX and $Apc^{Pirc/+}$+control groups. Black arrows indicate experimentally observed effects of their combination. Circles with slashes indicated no difference predicted for Apc^{WT}+OX group and $Apc^{Pirc/+}$+control groups. Data presented as mean ± s.e.m.

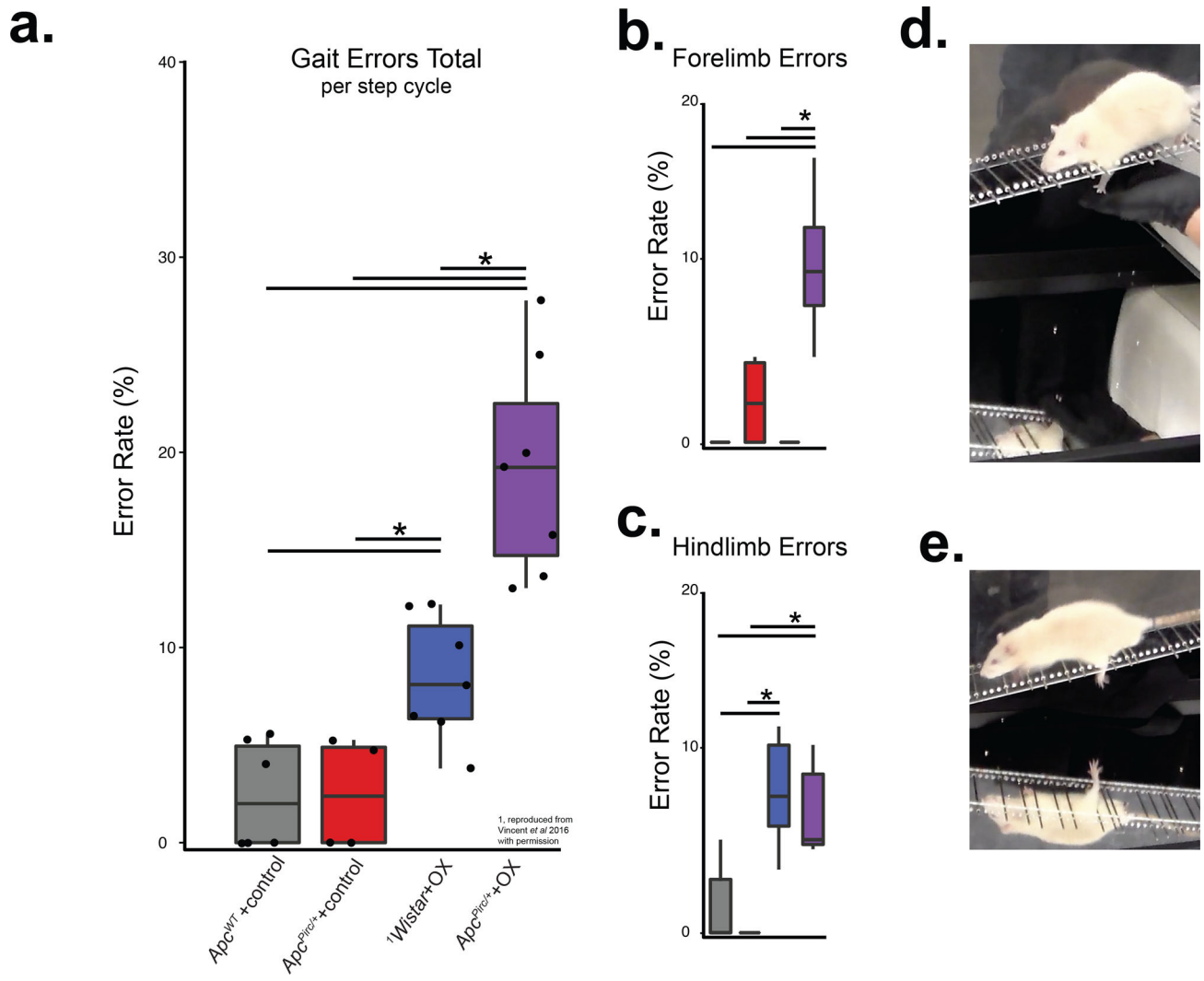

Figure 7. Behavioral dysfunction exacerbated by cancer-chemotherapy interaction.

a, Total gait errors as measured by secure fore- and hindfoot placement was scored by errors/step cycle during ladder rung walking. Recordings were analyzed from Apc^{WT} +control (n = 6), Wistar+OX (n = 7), $Apc^{Pirc/+}$+control (n = 4) and $Apc^{Pirc/+}$+OX (n = 7) animals. **b-c**, indicate the contributions of fore- (**b**) and hindlimb (**c**) errors to total error rates. **d**, Photograph shows left forelimb error in double image (simultaneous side and underneath views) of $Apc^{Pirc/+}$+OX rat walking on ladder rungs. **e**, Photograph shows left hind limb error in double image (simultaneous side and underneath views) of $Apc^{Pirc/+}$+OX rat walking on ladder rungs (representative cases of entire ladder rung walking trials can be viewed at Movie S1 and Movie S3 for Apc^{WT}+control and $Apc^{Pirc/+}$+OX rats respectively). * indicates statistically significant differences between experimental groups as empirically derived from hierarchical Bayesian model (stan_glm): 95% highest density intervals do not overlap between groupwise contrasts. [1]Wistar+OX data reproduced from Vincent et al 2016 with permission.